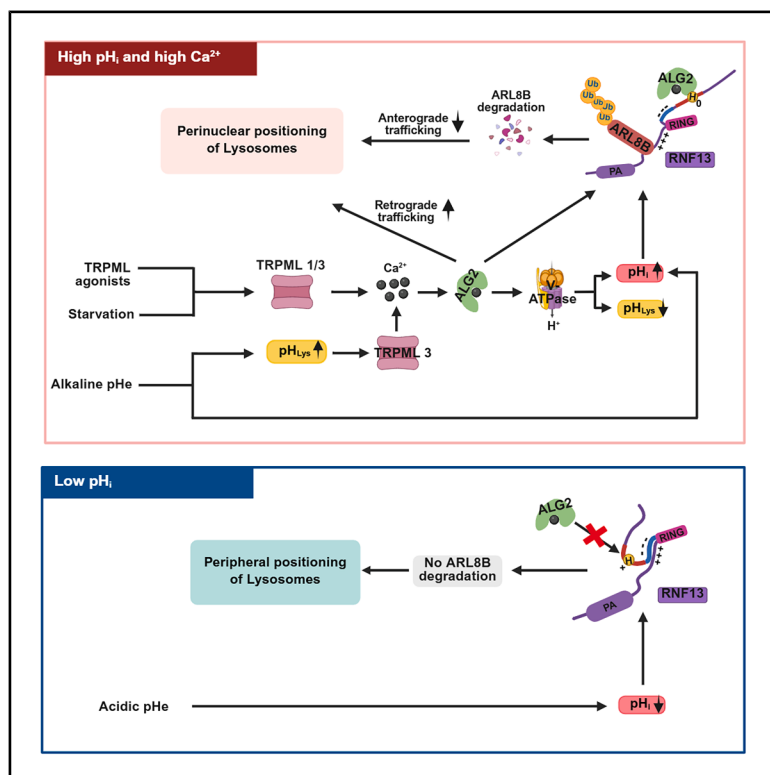


RNF13 mediates pH- and Ca²⁺-dependent regulation of lysosomal positioning

Graphical abstract



Authors

Lan Thi Trinh, Anh Van Vu,
Seunghye Shin, ..., Hyun Jin Kim,
Sungjoo Kim, Jong-Bok Yoon

Correspondence

sjkyoon@catholic.ac.kr (S.K.),
yoonj@yonsei.ac.kr (J.-B.Y.)

In brief

Trinh et al. identify RNF13 as a pH- and Ca²⁺-dependent regulator of lysosomal positioning via ubiquitin-mediated degradation of ARL8B. They show that starvation or alkaline extracellular pH enhances RNF13 activity, while acidic intracellular pH suppresses it. This reveals a mechanism by which Ca²⁺ signaling and pH dynamics regulate lysosomal transport.

Highlights

- RNF13 controls lysosomal positioning via ARL8B degradation
- RNF13 activity is regulated by intracellular pH and Ca²⁺ levels
- Starvation or alkaline pH_e enhances RNF13 activity; acidic pH_i suppresses it
- RNF13 dysfunction is linked to developmental and epileptic encephalopathy-73



Article

RNF13 mediates pH- and Ca²⁺-dependent regulation of lysosomal positioning

Lan Thi Trinh,¹ Anh Van Vu,¹ Seunghye Shin,² Chanaeng Lee,¹ Sang-Hee Park,¹ Eun-Bee Cho,² Yunseok Heo,³ Hyun Jin Kim,⁴ Sungjoo Kim,^{1,5,6,*} and Jong-Bok Yoon^{2,5,6,7,*}

¹Department of Medical Sciences, Graduate School of The Catholic University of Korea, Seoul 06591, Republic of Korea

²Department of Biochemistry, College of Life Science and Biotechnology, Yonsei University, Seoul 03722, Republic of Korea

³Biopharmaceutical Research Center, Korea Basic Science Institute (KBSI), Chungbuk 28119, Republic of Korea

⁴Department of Physiology, Sungkyunkwan University School of Medicine, Suwon 16419, Republic of Korea

⁵These authors contributed equally

⁶Senior author

⁷Lead contact

*Correspondence: sjkyoon@catholic.ac.kr (S.K.), yoonj@yonsei.ac.kr (J.-B.Y.)

<https://doi.org/10.1016/j.celrep.2025.116053>

SUMMARY

Environmental factors such as extracellular pH (pH_e) and nutrition status affect lysosomal localization and autophagy, but how pH_e , intracellular pH (pH_i), and Ca^{2+} regulate lysosome transport is not well understood. Here, we identify RNF13 as a key regulator of lysosomal positioning via pH_i - and Ca^{2+} -dependent degradation of ARL8B. Ca^{2+} -activated apoptosis-linked gene 2 (ALG-2) promotes retrograde lysosomal transport while increasing pH_i and decreasing lysosomal pH (pH_{lys}). Elevated pH_i deprotonates RNF13 at His332, enabling its interaction with Ca^{2+} -bound ALG-2 and inhibition of ARL8B-mediated anterograde transport. Alkaline pH_e elevates pH_{lys} and activates the lysosomal Ca^{2+} channel TRPML3, enhancing RNF13 activity and driving lysosomes toward a perinuclear position. Thus, starvation or alkaline pH_e induces ALG-2 activation and pH_i elevation, facilitating RNF13-mediated ARL8B degradation. In contrast, acidic pH_i suppresses RNF13, keeping ARL8B levels high even when ALG-2 is active. These findings reveal a coordinated mechanism involving Ca^{2+} signaling and pH dynamics in regulating lysosomal positioning.

INTRODUCTION

Lysosomes and late endosomes (collectively referred to as lysosomes) mediate the degradation of macromolecules from extracellular and intracellular sources via endocytosis and autophagy, respectively. Beyond degradation, lysosomes are crucial for energy metabolism and nutrient homeostasis by serving as signaling hubs.^{1–3} They are heterogeneous in size, shape, luminal pH, and subcellular localization. Perinuclear lysosomes are typically larger, more acidic, and exhibit greater degradative activity, while peripheral lysosomes are more motile.

Lysosomal positioning is tightly regulated and essential for diverse cellular functions, including autophagy, plasma membrane repair, antigen presentation, and cancer cell invasion.^{4–6} Their trafficking is governed by microtubule-based transport, inter-organelle interactions,^{7–9} and the membrane composition of phosphatidylinositol phosphates (PIPs).^{10–14} Kinesin motors drive anterograde movement toward the periphery, whereas dynein mediates retrograde transport to the perinuclear area. These opposing forces are coordinated by small guanosine triphosphate (GTP)ases and their effectors.^{15,16} For example, RAB7 promotes retrograde transport via RILP (Rab-interacting lysosomal protein),^{15,17} while RAB7-FYCO1 (FYVE and coiled-coil domain autophagy adaptor 1) interactions drive anterograde

movement. Other Rab GTPases (Rab26, Rab34, Rab36) also recruit RILP to promote perinuclear lysosomal clustering.^{18–22}

ARL8B (ARF-like GTPase 8B), a key GTPase for anterograde transport, interacts with kinesin-3 directly or with kinesin-1 via SKIP (also known as PLEKHM2).^{23–29} Its membrane localization is regulated by BORG.³⁰ ARL8B can also mediate retrograde transport through effectors such as RUFY3 (RUN and FYVE domain containing 3)^{31,32} or DENND6A (DENN domain containing 6A).³³ However, how RAB7 and ARL8B coordinate directional lysosome movement in response to stimuli remains unclear. The balance between these GTPases likely determines lysosomal positioning,³⁴ with peripheral lysosomes enriched in ARL8B and lower in RAB7.³⁴

Environmental cues such as extracellular pH (pH_e) and nutrient levels influence lysosomal distribution. Alkaline pH_e increases intracellular pH (pH_i),^{35–37} promoting perinuclear lysosome clustering^{38,39} and autophagy,³⁷ whereas acidic pH_e reverses these effects. Nutrient deprivation induces perinuclear localization to promote autophagosome fusion, while nutrient sufficiency supports peripheral positioning for mTORC1 activation.⁴⁰ Starvation triggers multiple regulators that contribute to perinuclear lysosome clustering,^{14,34,41–45} including elevated pH_i , which reduces ARL8B membrane association and enhances retrograde transport.⁴⁵ Yet mechanisms driving starvation-induced pH_i elevation and ARL8B redistribution remain poorly understood.



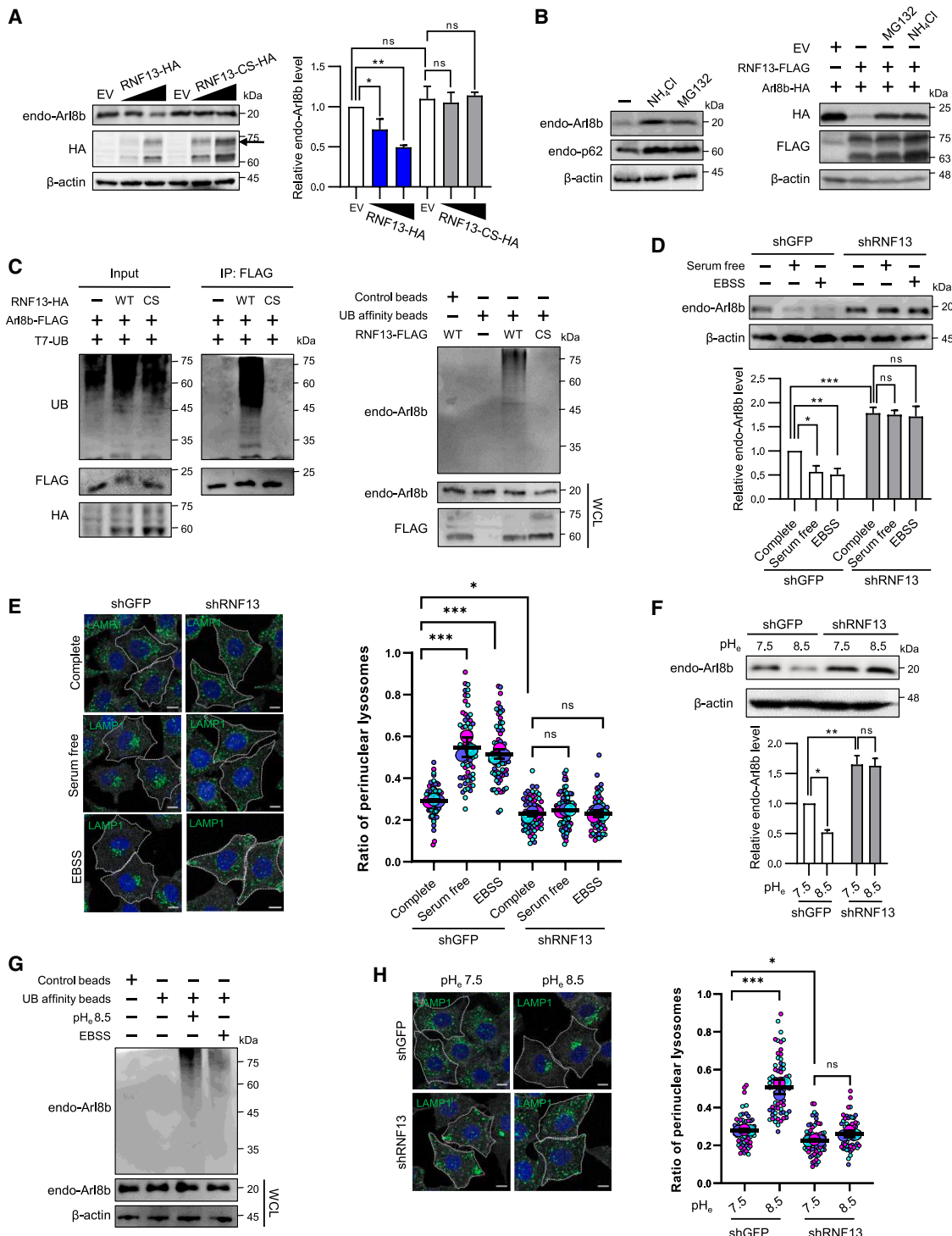


Figure 1. RNF13-promoted ARL8B degradation is required for starvation- and alkaline pH_e-induced perinuclear lysosomal positioning
(A) Western blot of endogenous ARL8B in HeLa cells transfected with an empty vector (EV), RNF13-HA, or RNF13 C243S (CS)-HA at increasing doses. Arrow indicates N-glycosylated RNF13. ARL8B was normalized to β-actin. Data are mean ± SD ($n = 3$). One-way ANOVA with Dunnett's test; ns, not significant; * $p < 0.05$; ** $p < 0.01$.

(B) Western blot of indicated proteins in HeLa cells treated with DMSO (–), MG132 (25 μM), or NH4Cl (20 mM) for 6 h. Left: control cells; right: cells cotransfected with ARL8B-HA and EV or RNF13-FLAG. Increased p62 confirms treatment efficacy.

(legend continued on next page)

Lysosomal Ca^{2+} release via TRPML1 (also known as MCOLN1) also influences lysosomal positioning during starvation. TRPML1 activates ALG-2, which recruits dynein in a Ca^{2+} -dependent manner.⁴¹ Increased cytosolic Ca^{2+} activates CaMKK β ⁴⁶ and calcineurin, promoting autophagy and TFEB (transcription factor EB) nuclear translocation.⁴⁷ TFEB targets include TMEM55B, which recruits JIP4 for dynein-dependent transport.⁴² However, it is unknown whether starvation-induced pH_i and lysosomal Ca^{2+} signaling converge to regulate perinuclear positioning (Figure S1A).

RING finger protein 13 (RNF13) is a type I transmembrane E3 ligase in the PA-TM-RING family, defined by a signal peptide, PA (protease-associaed) domain, TM (transmembrane) domain, and RING-finger motif.⁴⁸ RNF13 functions in muscle growth, neuronal development, and cancer.⁴⁹ Missense RNF13 variants are associated with developmental and epileptic encephalopathy-73 (DEE-73), a severe neurodevelopmental disorder linked to defective lysosomal localization.^{50,51} The molecular basis of DEE-73 remains elusive. Here, we investigate RNF13's role in regulating lysosomal positioning in response to pH_e and nutrient deprivation and explore its contribution to DEE-73 pathogenesis.

RESULTS

RNF13-promoted ARL8B degradation is required for starvation- or alkaline pH_e -induced perinuclear lysosomal positioning

To identify RNF13-specific ubiquitinated substrates, we used a proximity-dependent biotin-labeling method we previously developed.^{52–55} This approach employs a fusion of RNF13 and the biotin ligase BirA, which selectively biotinylates an acceptor peptide (AP) fused to ubiquitin (AP-Ub), enabling transfer of biotinylated AP-Ub to proximal substrates (Figure S1B). Streptavidin-based purification and proteomic analysis⁵² (see STAR Methods) identified ARL8B as a candidate RNF13 substrate (Figure S1C).

To validate RNF13-mediated ubiquitination and destabilization of ARL8B, HeLa cells were transfected with RNF13-hemagglutinin (HA), with or without ARL8B-FLAG. RNF13-HA reduced both endogenous and exogenous ARL8B levels in a dose-dependent manner, whereas the ligase-dead RNF13 C243S (RNF13 CS)-HA mutant had no effect (Figures 1A and S1D). Immunofluorescence confirmed this reduction in RNF13-expressing cells (Figure S1E). Proteasome inhibitor MG132 and lysosomal inhibitor NH_4Cl elevated endogenous ARL8B levels

and attenuated RNF13-mediated degradation of overexpressed ARL8B (Figure 1B), indicating involvement of both proteasomal and lysosomal pathways.

Polyubiquitin smears confirmed RNF13-dependent ubiquitination of ARL8B, absent with RNF13 CS (Figure 1C). RNF13 knockdown via small interfering RNA (siRNA) increased endogenous ARL8B levels (Figure S1F), consistent with negative regulation. This was also validated in MCF7 cells (Figure S1G). To confirm the specificity of ubiquitination, we generated ARL8B lysine mutants (K131R, K141R, and K146R). RNF13 did not reduce protein levels or ubiquitinate the 3KR mutant (Figures S1H and S1I), identifying these residues as primary ubiquitination sites. Together, these data demonstrate that RNF13 targets ARL8B for ubiquitination and degradation.

As ARL8B promotes peripheral lysosomal localization and its depletion induces perinuclear clustering,³⁰ we examined the impact of RNF13. RNF13 overexpression caused perinuclear clustering, while RNF13 knockdown dispersed lysosomes (Figures S1J–S1L). Given that ARL8B knockdown promotes autophagosome-lysosome fusion and autophagic degradation,⁴⁵ we assessed autophagy markers. RNF13 knockdown elevated p62 and LC3 levels, suggesting impaired autophagic flux (Figure S2A), whereas RNF13 overexpression reduced these markers (Figure S2B). Autophagosome-lysosome fusion assays showed that ARL8B overexpression and RNF13 knockdown suppressed fusion, while ARL8B depletion or RNF13 overexpression enhanced it (Figures S2C and S2D). These findings suggest RNF13 regulates autophagy by modulating ARL8B.

Lysosomal positioning influenced by starvation and pH_i have been linked to alterations of ARL8B levels on lysosomes.⁴⁵ To investigate RNF13's role in this process, we generated stable RNF13 knockdown MCF7 cells. EBSS or serum-free media reduced ARL8B levels in control cells, but not in RNF13-depleted cells (Figure 1D). Starvation induced perinuclear lysosomal clustering in control cells, but lysosomes remained dispersed in RNF13 knockdown cells (Figure 1E). Transient ARL8B depletion induced clustering in both control and RNF13-depleted cells (Figures S3A and S3B), suggesting that elevated ARL8B levels mediate the lysosomal dispersal phenotype upon RNF13 knockdown.

To examine pH_e effects, we incubated cells at different pH_e values and confirmed corresponding shifts in pH_i (Figures S3C and S3D). In control cells, ARL8B levels decreased at pH_e 8.5 compared to pH_e 7.5, whereas no reduction was observed in

(C) Ubiquitination assay of ARL8B. Left: HeLa cells cotransfected with ARL8B-FLAG, T7-UB, and EV, RNF13-HA, or CS-HA. Lysates were immunoprecipitated with FLAG and immunoblotted. Right: lysates from cells transfected with EV, RNF13-FLAG, or CS-FLAG incubated with ubiquitin-affinity or control beads. All cells were pretreated with MG132 (25 μM , 6 h). Blots probed with indicated antibodies.

(D) Western blot of ARL8B in MCF7 cells expressing shGFP or shRNF13 after 2 h in complete, EBSS, or serum-free media. ARL8B was normalized to β -actin. Mean \pm SD ($n = 3$). Two-way ANOVA with Tukey's test; ns, not significant; * $p < 0.05$; ** $p < 0.01$; *** $p < 0.001$.

(E) Left: immunofluorescence of LAMP1 (lysosomes), CD147 (cell boundary), and DAPI (nuclei) in samples from (D). Scale bar, 10 μm . Right: SuperPlot of perinuclear/total LAMP1 ratio from shell analysis (see STAR Methods). Each condition includes 3 experiments (>20 cells/experiment). Small circles, individual cells; large circles, experimental means; bars, mean \pm SD ($n = 3$). Two-way ANOVA with Tukey's test: ns, not significant; * $p < 0.05$; ** $p < 0.01$.

(F) Western blot of ARL8B in shGFP or shRNF13 MCF7 cells after 2 h in alkaline media. ARL8B was normalized to β -actin. Mean \pm SD ($n = 3$). Two-way ANOVA with Tukey's test.

(G) Ubiquitination assay of endogenous ARL8B in HeLa cells treated as indicated. Cells were pretreated with MG132 as in (C). Lysates were incubated with control or ubiquitin-affinity beads and analyzed by Western blot.

(H) Left: immunofluorescence of LAMP1, CD147, and DAPI in cells from (F). Scale bar, 10 μm . Right: SuperPlot of perinuclear/total LAMP1 ratio as in (E). Data are mean \pm SD from three experiments. Two-way ANOVA with Tukey's test: ns, not significant; * $p < 0.05$; ** $p < 0.001$.

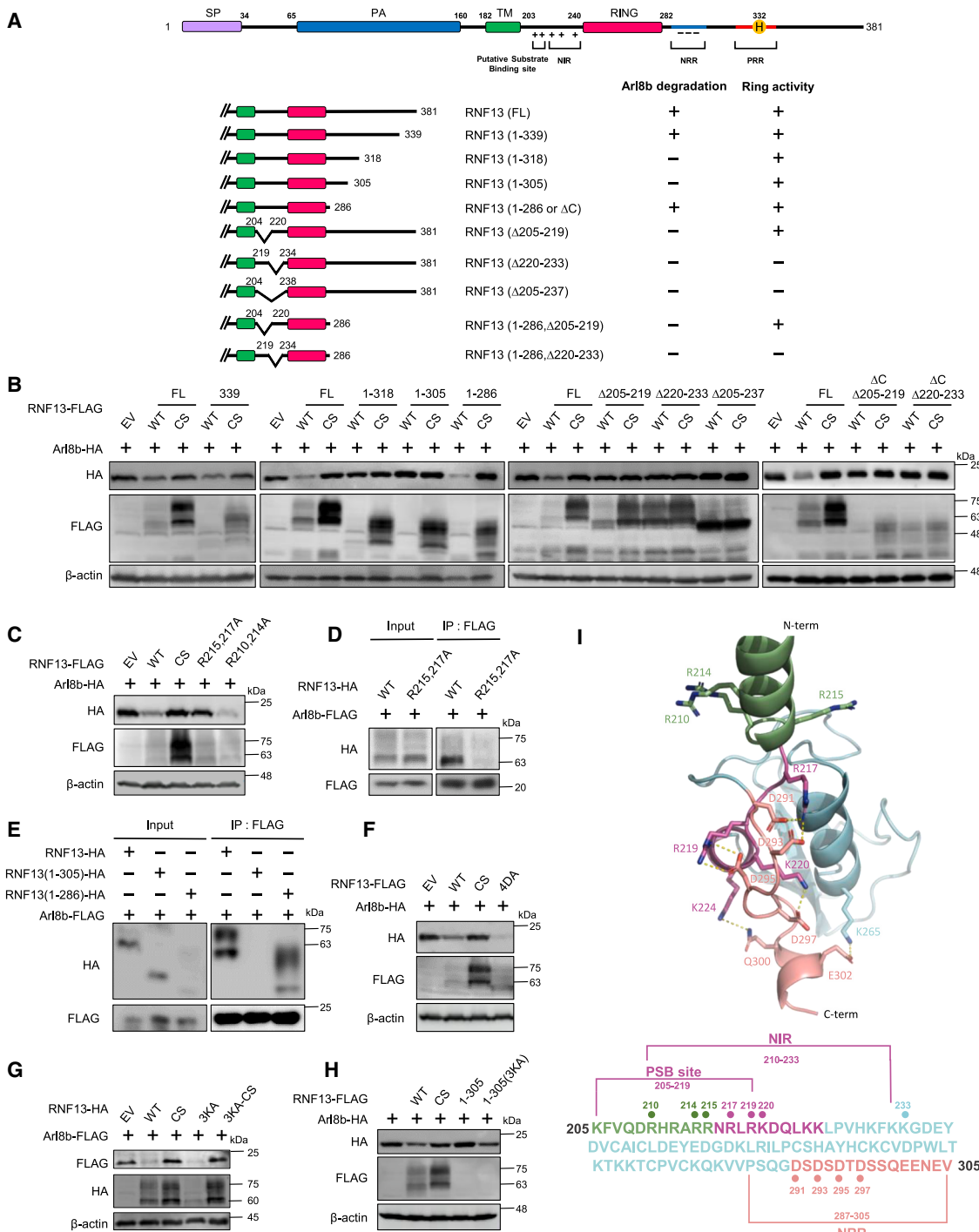


Figure 2. C-terminal tail of RNF13 regulates its activity toward ARL8B

(A) Schematic of RNF13 constructs showing domain organization and activity in ARL8B degradation and RING ligase function. SP, signal peptide; PA, protease-associated domain; TM, transmembrane; RING, RING finger domain; NRR, negative regulatory region; NIR, NRR-interacting region; PRR, positive regulatory region; His332, proposed pH sensor.

(B–H) Western blot analysis of ARL8B and indicated RNF13 constructs: (B and C) HeLa cells cotransfected with ARL8B-HA and the indicated RNF13 constructs for 24 h; (D and E) HeLa cells cotransfected with ARL8B-FLAG and RNF13 constructs, followed by MG132 treatment (25 μM, 6 h) and FLAG immunoprecipitation; (F and G) HeLa cells overexpressing ARL8B with indicated RNF13 constructs; (H) HeLa cells cotransfected with ARL8B-HA and RNF13 variants. EV, empty vector; WT, wild type; CS, C243S; 4DA, D291/293/295/297A; 3KA, K220/224/233A.

(legend continued on next page)

RNF13 knockdown cells (Figure 1F). MG132 or NH₄Cl treatment blocked RNF13-mediated ARL8B degradation under alkaline pH_e or starvation (Figure S3E). These treatments also increased ARL8B ubiquitination (Figure 1G). RNF13 knockdown inhibited perinuclear lysosomal clustering induced by alkaline pH_e (Figure 1H). Together, these findings suggest that RNF13 is required for starvation- and alkaline pH_e-induced perinuclear lysosomal repositioning by regulating ARL8B.

To analyze lysosome redistribution kinetics and ARL8B dynamics, we used time-lapse confocal microscopy in cells coexpressing LAMP1-GFP and ARL8B-mCherry. Colocalization during cytoplasmic trafficking confirmed their lysosomal association (Video S1; Figure S3F). Both pH 8.5 and serum-free media induced perinuclear localization of LAMP1-GFP and ARL8B-mCherry (Figure S3F, upper panel), with ARL8B-mCherry fluorescence decreasing while LAMP1-GFP remained constant (Figure S3G).

Time-lapse imaging showed progressive perinuclear lysosome clustering and decreased ARL8B-mCherry fluorescence over 1 h post-treatment with alkaline pH_e or starvation (Videos S2 and S3; Figure S3H). Cells in control media also showed slight fluorescence loss, likely due to photobleaching, not degradation, as protein levels remained unchanged by immunoblotting (Figure S3G). RNF13 knockdown markedly impaired lysosomal redistribution and ARL8B-mCherry reduction in response to alkaline pH_e (Videos S2 and S4–S6; Figure S3I). These results support a strong correlation between ARL8B degradation and lysosomal repositioning.

We previously reported RNF167 also influences ARL8B levels.⁵⁴ To distinguish roles of RNF13 and RNF167 in pH_e-induced lysosomal dynamics, we compared their individual and combined knockdown effects. Unlike RNF13 knockdown, RNF167 depletion did not severely impair alkaline pH_e-induced lysosomal clustering. Dual knockdown resembled RNF13 depletion alone, with a more pronounced effect than RNF167 knockdown (Figure S3J). Time-lapse imaging confirmed this (Video S7 vs. S5 and S6). Alkaline pH_e caused greater reductions in ARL8B-mCherry and total ARL8B levels in control and RNF167-depleted cells compared to RNF13-depleted cells (Figure S3K). Furthermore, unlike RNF13, RNF167's regulation of ARL8B was insensitive to acidic pH_e (Figure S3L). These findings underscore the critical role of RNF13 in controlling ARL8B stability and lysosomal positioning in response to physiological cues that affect pH_i. Based on these findings, we focused subsequent analyses on dissecting the upstream mechanisms governing RNF13 activation.

C-terminal tail of RNF13 regulates its activity toward ARL8B

To define regions of RNF13 essential for ARL8B degradation, we used a series of deletion mutants (Figures 2A and 2B). RNF13 (1–339) degraded ARL8B similarly to full-length RNF13, whereas RNF13 (1–318) and RNF13 (1–305) did not. Notably, RNF13 (1–286), lacking the C-terminal sequence beyond the RING

domain, retained ARL8B-degrading activity. Ligase-dead C243S versions of these C-terminal truncations accumulated to higher levels than their wild-type counterparts. MG132 treatment increased abundance of C-terminal deletion mutants (Figure S4A), indicating intact RING-dependent auto-ubiquitination and folding. These findings suggest RNF13 (1–286) is sufficient for ARL8B recognition and ubiquitination, while the unstructured C-terminal region predicted by AlphaFold⁵⁵ may regulate RNF13 activity.

Deletion analysis also revealed opposing regulatory functions within the C-terminal region. The segment spanning residues 319–339, termed the positive regulatory region (PRR), promoted ARL8B degradation, whereas the 287–305 region, termed the negative regulatory region (NRR), suppressed it. Internal deletion mutants RNF13 (Δ205–237) and RNF13 (Δ220–233) lacked both auto-degradation and ARL8B degradation activity, while RNF13 (Δ205–219) and RNF13 (1–286, Δ205–219) retained RING activity but failed to degrade ARL8B (Figure 2B). A mutant with R215A and R217A substitutions also showed impaired ARL8B degradation and interaction (Figures 2C and 2D), identifying these residues as critical for ARL8B recognition.

Coimmunoprecipitation showed that while full-length RNF13 and RNF13 (1–286) bound ARL8B, RNF13 (1–305), containing NRR but not PRR, did not (Figure 2E). The NRR is highly acidic (7 of 19 residues are negatively charged; none are positive). To test its role, we substituted four Asp residues (D291, D293, D295, D297) with Ala (4DA), which enhanced ARL8B degradation (Figure 2F). In addition, a region between the transmembrane and RING domains (residues 210–233) contains a basic stretch with 12 positively charged residues. A triple Lys-to-Ala mutant (K220A, K224A, K233A, “3KA”) in both full-length RNF13 and RNF13 (1–305) also increased ARL8B degradation (Figures 2G and 2H). Unlike R215A/R217A, the RNF13 CS 3KA mutant still interacted with ARL8B (Figure S4B), suggesting K220, K224, and K233 modulate intramolecular regulation rather than substrate binding. These data support a model in which ionic interactions between the acidic NRR and the adjacent basic region—designated the NRR-interacting region (NIR)—inhibit ARL8B binding, possibly by sterically blocking the overlapping binding site.

Given the availability of RNF13's crystal structure (residues 216–290) and a high-confidence AlphaFold model for residues 182–224,⁵⁶ we utilized GalaxyWEB (<https://galaxy.seoklab.org/>) to dock NRR residues (291–305) into the composite structure. The predicted model suggests that the NRR interacts with a basic surface overlapping the ARL8B-binding region (Figure 2I), supporting a mechanism in which intramolecular interactions repress RNF13 activity under basal conditions and are relieved under stress such as starvation or alkaline pH_i.

Histidine 332 acts as a pH sensor to regulate pH-dependent activity of RNF13

Given that cytosolic alkalinization reduces ARL8B levels in an RNF13-dependent manner, we examined whether RNF13

(I) Predicted structure of RNF13 (aa 205–305) modeled as a ribbon diagram. The N-terminal helix (aa 205–215, green), basic-rich region (216–225, magenta), acidic-rich region (291–305, salmon), and remaining residues (cyan) are shown. Salt bridges (R217–D291/D293, R219–D295, K220–D297, and K265–E302) and a hydrogen bond (K224–Q300) are indicated by yellow dotted lines. The corresponding sequence is shown with annotated regions (PSB, NIR, NRR) and key residues marked.

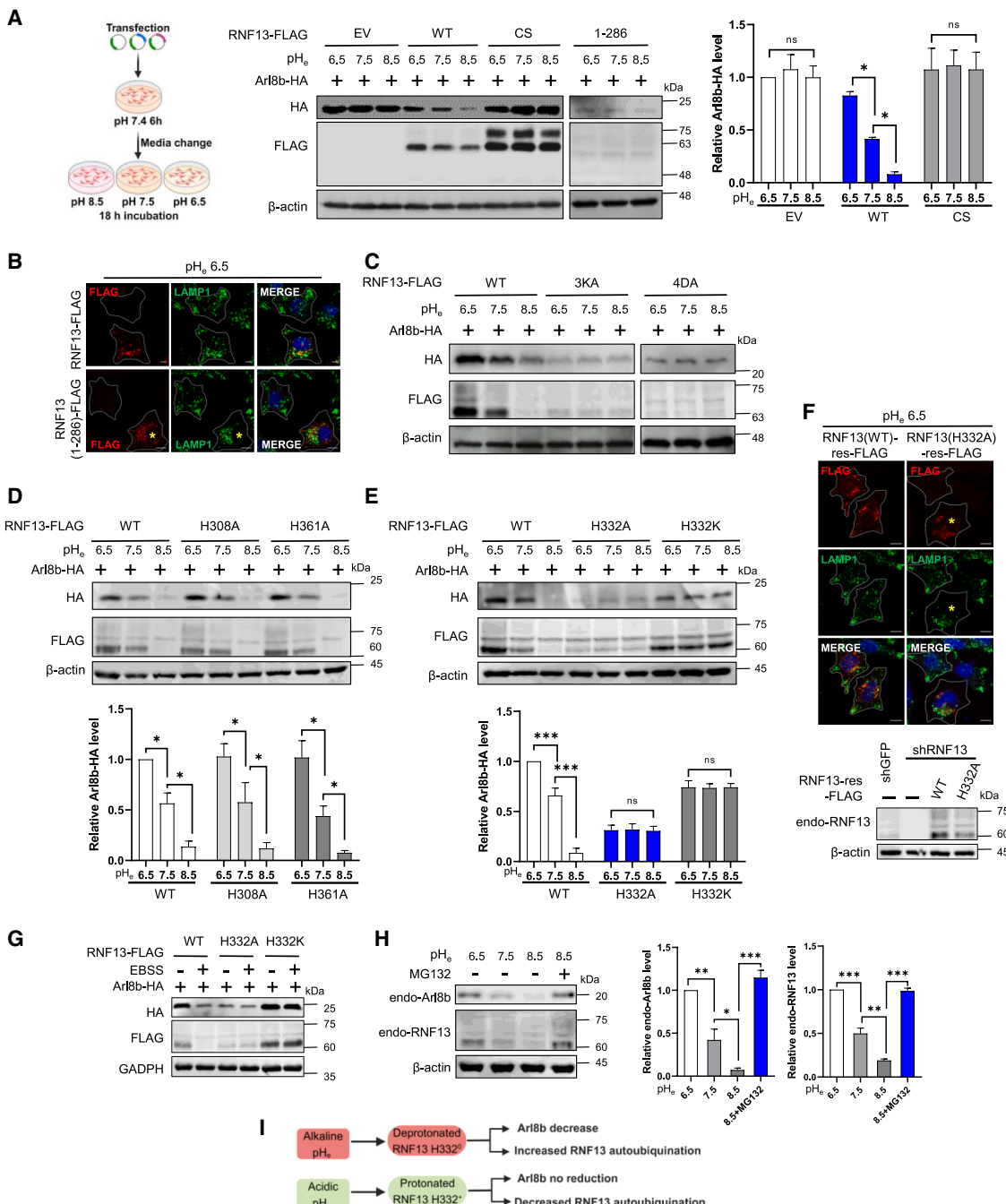


Figure 3. Histidine 332 acts as a pH sensor to regulate the pH-dependent activity of RNF13

(A) Schematic of the experimental setup (left) and Western blot of lysates from HeLa cells cotransfected with ARL8B-HA and either EV, RNF13-FLAG, RNF13 CS-FLAG, or RNF13 (1-286)-FLAG. Six hours post-transfection, cells were incubated in media at pH 6.5, 7.5, or 8.5 for 18 h. ARL8B-HA levels were normalized to β-actin and shown as mean ± SD ($n = 3$). Two-way ANOVA with Tukey's test; ns, not significant; * $p < 0.05$.

(B) Immunofluorescence of indicated proteins in HeLa cells transfected with RNF13-FLAG or 1-286-FLAG. Yellow asterisks mark cells with perinuclear lysosome positioning. Scale bar, 10 μm.

(C) Western blot of indicated proteins from HeLa cells transfected with the indicated constructs for 6 h and incubated in media of varying pH for 18 h.

(D and E) Western blot and quantification of ARL8B-HA coexpressed with RNF13 histidine mutants. Protein levels were normalized to β-actin. Data are mean ± SD ($n = 3$). Two-way ANOVA with Tukey's test; ns, not significant; * $p < 0.05$; *** $p < 0.001$.

(F) Immunofluorescence (top) and Western blot (bottom) of shRNF13 HeLa cells transfected with shRNA-resistant wild-type RNF13 or RNF13 H332A. Cells were incubated in pH 6.5 media for 18 h following 6 h transfection. Scale bar, 10 μm.

(G) Western blot of indicated proteins in HeLa cells cotransfected with ARL8B-HA and either WT or mutant RNF13 after 2 h in EBSS.

(legend continued on next page)

activity toward ARL8B is modulated by cytosolic pH. HeLa cells transfected with epitope-tagged RNF13 and ARL8B were first cultured at pH 7.4 for 6 h, then shifted to media of varying pH for 18 h. ARL8B-HA levels decreased with increasing pH_e in the presence of wild-type RNF13-FLAG (Figure 3A). In contrast, ARL8B levels were largely unaffected when coexpressed with ligase-dead RNF13 (RNF13 CS) or empty vector, indicating that RNF13 activity is pH sensitive.

Truncated RNF13 (1–286) exhibited pH-independent ARL8B degradation and was more active than full-length RNF13 at pH 6.5 (Figure 3A). Consistently, only RNF13 (1–286), and not full-length RNF13, induced perinuclear lysosome clustering under acidic conditions (Figure 3B). Mutants RNF13 3KA and 4DA, which likely disrupt NRR-NIR interactions, also showed enhanced, pH-independent activity (Figure 3C), suggesting that the C-terminal region—particularly NRR—plays a pivotal role in pH-dependent regulation.

Histidines, with near-neutral pKa values, often act as physiological pH sensors. To test whether RNF13 C-terminal His residues mediate pH responsiveness, we generated substitution mutants at H308, H332, and H361. RNF13 H308A and H361A retained pH-sensitive degradation of ARL8B and themselves, similar to wild-type RNF13 (Figure 3D). In contrast, H332A and H332K mutants were pH insensitive: both failed to respond to alkaline pH_e and did not undergo self-degradation or promote ARL8B degradation in a pH-dependent manner (Figure 3E).

Importantly, RNF13 H332A, but not the wild-type protein, induced perinuclear lysosomal clustering at pH_e 6.5 (Figure 3F), suggesting that this variant retains activity even under acidic conditions. Given that starvation elevates cytosolic pH, incubation in EBSS decreased levels of wild-type RNF13 and coexpressed ARL8B, but this effect was abolished in H332A and H332K mutants (Figure 3G). Analysis of endogenous RNF13 and ARL8B further showed reduced protein levels at higher pH_e (Figure 3H).

Together, these findings support a model in which His332 within the PRR functions as a pH sensor. Deprotonation of H332 may activate RNF13, enhancing both its auto-ubiquitination and its activity toward ARL8B (Figure 3I). This activation could occur directly, by modulating intramolecular interactions such as the NRR-NIR contact, or indirectly, via recruitment of a regulatory factor that disrupts this inhibitory interface.

RNF13 is essential for TRPML1-mediated retrograde lysosomal transport

Starvation not only elevates pH_i but also activates the lysosomal Ca²⁺ channel TRPML1, which recruits the Ca²⁺-binding protein ALG-2 to lysosomes. ALG-2 interacts with the dynein-dynein complex to promote retrograde lysosomal transport.⁴¹ To examine whether RNF13 mediates TRPML1-dependent transport, we treated control and RNF13-knockdown cells with the TRPML agonist ML-SA1. In control cells, ML-SA1 reduced ARL8B protein levels, an effect absent in RNF13 knockdown

cells (Figure 4A). Similarly, ML-SA1 induced perinuclear lysosomal accumulation in control but not RNF13-depleted cells (Figures 4B, S3F, and S3G; Video S8), suggesting that RNF13 is required for ML-SA1-induced retrograde lysosome trafficking via ARL8B degradation.

Given the reduced RNF13 activity at acidic pH_i, we tested whether ML-SA1 could promote lysosome clustering under acidic pH_e 6.5. Although ML-SA1 induced TFEB nuclear translocation at pH_e 6.5, confirming TRPML1 activation (Figure S4C), it failed to promote perinuclear lysosome positioning (Figure S4D). Additionally, ML-SA1 did not reduce ARL8B levels at pH_e 6.5, in contrast to its effect at pH_e 7.5 (Figure S4E). These results indicate that TRPML1 activation alone is insufficient for retrograde lysosomal transport under acidic conditions, likely due to impaired RNF13 activity.

The TRPML antagonist ML-SI3 inhibited lysosomal clustering induced by serum starvation or ML-SA1 and blocked alkaline pH_e-induced perinuclear redistribution (Figure S4F). ML-SI3 concurrently prevented the ARL8B reduction caused by these treatments (Figure S4G), implicating lysosomal Ca²⁺ release as a critical trigger for RNF13 activation in response to alkaline pH_e or starvation.

Previous studies reported that ALG-2 overexpression promotes perinuclear lysosome positioning, while its loss results in peripheral distribution.⁴¹ We investigated whether ALG-2 regulates ARL8B levels. Overexpression of ALG-2 reduced both exogenous and endogenous ARL8B (Figure 4C), whereas ALG-2 knockdown increased endogenous ARL8B (Figure 4D). Moreover, ALG-2 depletion blocked the decrease in RNF13 and ARL8B levels following alkaline pH_e treatment (Figure 4E) and starvation-induced ARL8B reduction (Figure 4F). It also suppressed perinuclear lysosome clustering under starvation or alkaline pH_e conditions (Figure 4G). To determine if this phenotype was driven by elevated ARL8B, we performed double knockdown of ALG-2 and ARL8B. Perinuclear clustering was restored, suggesting that increased ARL8B levels underlie the peripheral lysosome positioning in ALG-2-depleted cells (Figure 4H). Together, these findings indicate that RNF13-mediated ARL8B degradation and retrograde lysosome transport depend on lysosomal Ca²⁺ release and the Ca²⁺-responsive adaptor ALG-2 (Figure 4I).

Starvation induces cytoplasmic alkalinization in a TRPML- and ALG-2-dependent manner

Given the pH sensitivity of RNF13 and its requirement for ML-SA1-induced retrograde lysosomal transport, we examined whether TRPML activation alters pH_i and modulates RNF13 activity. Cytosolic pH was monitored using a ratiometric probe composed of pH-sensitive super-ecliptic pHluorin and pH-insensitive mCherry^{57,58} (Figure S5A). Starvation with EBSS induced a time-dependent increase in pH_i, rising from 7.4 to 7.8 after 2 h (Figure 5A). ML-SA1 treatment also elevated pH_i in complete media to a similar extent (Figure 5B). In both cases,

(H) Western blot and quantification of endogenous ARL8B and RNF13 in HeLa cells cultured at different pH for 18 h with or without MG132 (25 μM, 6 h). Protein levels are normalized to β-actin; data are mean ± SD ($n = 3$). Two-way ANOVA with Tukey's test: * $p < 0.05$, ** $p < 0.01$, *** $p < 0.001$.

(I) Summary of H332's role as a pH sensor regulating pH-dependent RNF13 activity.

Created with BioRender.com.

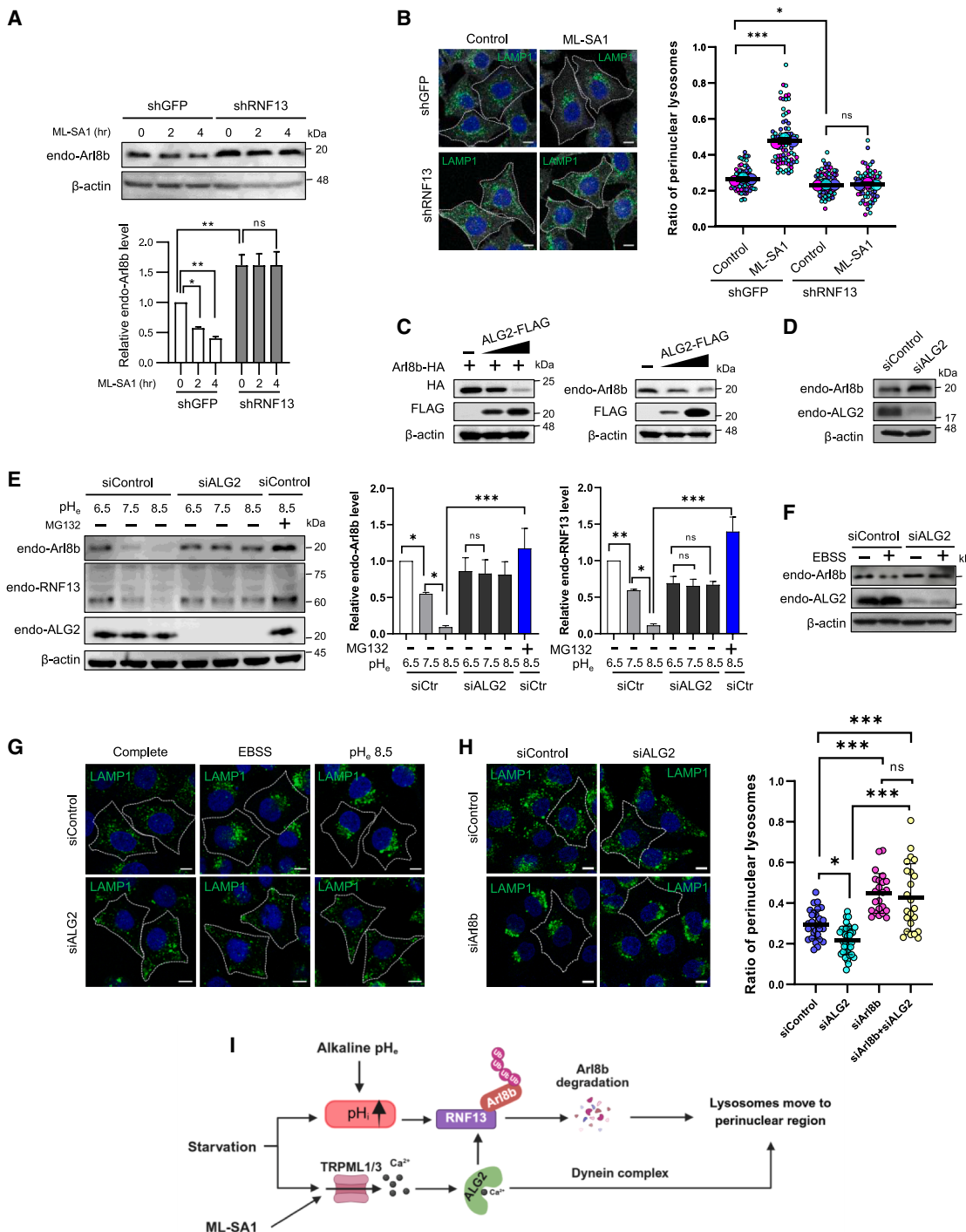


Figure 4. RNF13 is essential for retrograde lysosomal transport induced by a TRPML agonist

(A) Western blot and quantification of endogenous ARL8B in MCF7 cells expressing shGFP or shRNF13 treated with ML-SA1 (25 μM) for 0, 2, or 4 h. ARL8B levels normalized to β-actin. Data are mean ± SD ($n = 3$). Two-way ANOVA with Tukey's test; ns, not significant; * $p < 0.05$; ** $p < 0.01$.

(B) Left: Immunofluorescence of LAMP1 in samples from (A) after 2 h. Scale bar, 10 μm. Right: SuperPlot of perinuclear/total LAMP1 ratio from shell analysis ($n = 3$). Two-way ANOVA with Tukey's test; ns, not significant; ** $p < 0.01$; *** $p < 0.001$.

(C) Western blot of HeLa cells transfected with increasing FLAG-ALG-2, with or without ARL8B-HA. Blots probed with indicated antibodies.

(D) Western blot of endogenous ARL8B and ALG-2 in HeLa cells transfected with control or ALG-2 siRNA for 72 h.

(legend continued on next page)

this alkalinization was fully blocked by bafilomycin A1 (BafA1), a V-ATPase inhibitor (Figure 5C), suggesting that V-ATPase is likely involved in the pH_i increase triggered by starvation or TRPML activation.

To assess whether EBSS or ML-SA1 also alters lysosomal pH (pH_{lys}), we used a pH_{lys} reporter cell line expressing mTFP1 in the lysosomal lumen and mCherry on the cytosolic face⁵⁹ (Figure S5B). Both treatments reduced pH_{lys} from 4.7 to below 4.3 (Figure 5D), indicating a simultaneous lysosomal acidification and cytosolic alkalinization. Notably, ML-SI3, a TRPML antagonist, reduced basal pH_i to 7.2 and blocked the EBSS- and ML-SA1-induced increases (Figures 5E; S5C and S5D), implicating TRPML channel activity as a key player of these pH shifts.

Consistent with a recent report,⁶⁰ Torin1, an mTOR inhibitor, also lowered pH_{lys} (Figure 5D), likely via upregulation of V-ATPase assembly. In parallel, Torin1 increased pH_i (Figure 5E), an effect blocked by ML-SI3, suggesting that mTOR inhibition induces cytosolic alkalinization via TRPML channel activation. Cotreatment with Torin1 and ML-SA1 failed to produce an additive effect on pH_i, implying convergence on a shared pathway (Figure 5E).

We next assessed the role of ALG-2 in pH regulation. Overexpression of wild-type ALG-2, but not a Ca²⁺-binding-deficient mutant, led to cytosolic alkalinization and lysosomal acidification (Figures S5E and S5F). Furthermore, ALG-2 knockdown suppressed the ML-SA1-induced increase in pH_i (Figure 5F), indicating that Ca²⁺-activated ALG-2 is required for TRPML-mediated cytosolic alkalinization. Similarly, ALG-2 depletion blocked Torin1-induced pH_i elevation (Figure 5G). Overall, these findings suggest that starvation triggers TRPML channel-dependent activation of ALG-2, which enhances V-ATPase activity, leading to a simultaneous decrease in pH_{lys} and increase in pH_i (Figure 5H).

Ca²⁺-bound ALG-2 activates RNF13 via a His332 deprotonation-dependent interaction with PRR that relieves NRR-mediated repression

Since Ca²⁺-bound ALG-2 is essential for RNF13 activation, we monitored cytosolic Ca²⁺ levels using the GCaMP6f sensor.⁶¹ EBSS and ML-SA1 treatments led to a sustained increase in GCaMP6f signals over 2 h (Figures 6A, 6B, and S6A). We next compared cytosolic Ca²⁺ and pH_i after 2 h of treatment with ML-SA1, EBSS, serum-free media, or Torin1 (Figure 6C). Starvation and ML-SA1 elevated Ca²⁺ signals ($\Delta F/F_0 = 0.44\text{--}0.63$), whereas Torin1 produced only a minor increase ($\Delta F/F_0 \leq 0.11$). All four conditions raised pH_i to ~7.8. Thus, starvation and ML-SA1 elicit greater Ca²⁺ elevation than mTOR inhibition. Notably, Torin1 failed to reduce ARL8B levels or significantly affect lysosomal positioning^{44,55} (Figure S6B).

We next tested whether increased cytosolic Ca²⁺ could compensate for Torin1's limited effect on RNF13 activation. Thapsigargin, a SERCA inhibitor, raised Ca²⁺ but not pH_i (Figure S6C). While thapsigargin alone had minimal effect, its cotreatment with Torin1 reduced ARL8B levels and triggered perinuclear lysosome clustering (Figure S6B). This indicates that Torin1-induced pH_i alkalinization requires elevated cytosolic Ca²⁺ for RNF13 activation.

To explore the mechanism of Ca²⁺-ALG-2-mediated RNF13 activation, we performed coimmunoprecipitation (coIP) assays. Both overexpressed and endogenous RNF13 interacted with ALG-2 in a Ca²⁺-dependent manner (Figures 6D and 6E). ALG-2 overexpression enhanced RNF13 binding (Figure 6F), whereas the Ca²⁺-binding-deficient ALG-2 mutant (ALG-2-FLAG^{EEAA}) failed to bind RNF13 (Figure 6G). RNF13 constructs lacking the PRR (residues 1–318 or 1–286) were also unable to interact with ALG-2, unlike full-length RNF13 (Figure 6H).

Importantly, ALG-2 pulled down more RNF13 at pH 8.5 than at pH 6.5 (Figure 6I), suggesting that PRR-ALG-2 interaction is enhanced by His332 deprotonation. Supporting this, ALG-2 bound more strongly to RNF13-H332A than to the wild-type but failed to interact with RNF13-H332K (Figure 6J), suggesting that histidine protonation status regulates binding affinity.

We then examined whether ALG-2 mediates the interaction between RNF13 and ARL8B. ALG-2 knockdown significantly reduced the RNF13-ARL8B interaction (Figure 6K). Interestingly, the H332A mutant showed enhanced ARL8B binding, whereas the H332K mutant displayed weaker interaction compared to wild-type RNF13 (Figure 6L). These findings suggest that ALG-2 binding to RNF13 promotes its association with ARL8B.

Based on these results, we propose a model wherein acidic pH_i or low cytosolic Ca²⁺ limits ALG-2 binding to the PRR. This allows the NRR to intramolecularly engage the NIR, which overlaps the ARL8B binding site, thus blocking RNF13-ARL8B interaction and leading to ARL8B stabilization and peripheral lysosomal distribution. In contrast, elevated Ca²⁺ and alkaline pH_i favor H332 deprotonation and PRR-ALG-2 binding, which relieves NRR-mediated repression of the NIR. This enables RNF13 to interact with ARL8B, leading to its ubiquitination and degradation, and promotes perinuclear lysosome positioning (Figure 6M). Given that RNF13 auto-ubiquitination is modulated by pH_i and Ca²⁺, these conformational changes may also regulate access to ubiquitin-loaded E2 enzymes.

Alkaline pH_e increases cytosolic Ca²⁺ via TRPML3 activation

Given that alkaline pH_e induces RNF13- and ALG-2-dependent perinuclear lysosomal clustering, we examined whether it also

(E) Western blot and quantification of ARL8B and RNF13 in cells treated as in (D), then cultured in media at pH 6.5, 7.5, or 8.5 for 18 h. MG132 (25 μM) added to siControl cells 6 h prior to collection. Protein levels normalized to β-actin. Data are mean ± SD ($n = 3$). Two-way ANOVA with Tukey's test; ns, not significant; * $p < 0.05$; ** $p < 0.01$; *** $p < 0.001$.

(F) Western blot of ARL8B and ALG-2 in HeLa cells transfected with control or ALG-2 siRNA and incubated for 2 h in complete or EBSS media.

(G) Immunofluorescence of LAMP1 showing lysosome positioning under EBSS or alkaline pH_e in cells with or without ALG-2 knockdown.

(H) Left: immunofluorescence of LAMP1 in HeLa cells transfected for 72 h with control siRNA, siALG-2, siARL8B, or both. Right: perinuclear/total LAMP1 ratio quantified by shell analysis (>20 cells/condition). Data are mean ± SD; one-way ANOVA with Tukey's test: ns, not significant; * $p < 0.05$; *** $p < 0.001$.

(I) Model: RNF13-mediated ARL8B degradation promotes perinuclear lysosome accumulation upon ML-SA1 or starvation.

Created with BioRender.com.

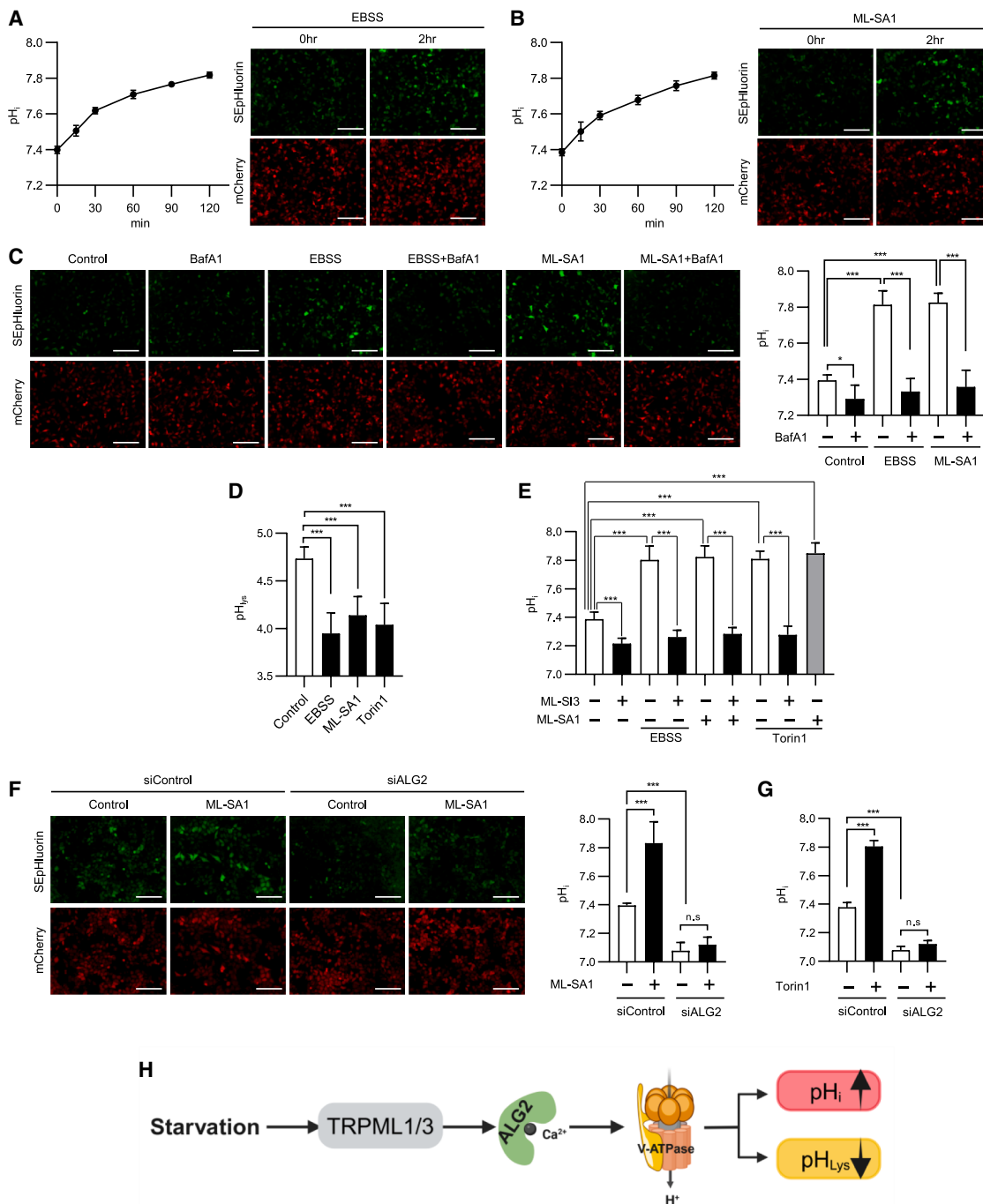


Figure 5. Starvation induces cytoplasmic alkalinization in a TRPML- and ALG-2-dependent manner

(A and B) pH_i in HeLa cells expressing mCherry-SEpHluorin after 2 h in EBSS (A) or ML-SA1 (25 μM) (B). SEpHluorin/mCherry fluorescence ratios were converted to pH_i using a calibration curve (Figure S5A). Mean pH_i ± SD calculated from three replicates.

(C) pH_i measurement in sensor cells after 2 h incubation with DMSO, EBSS, or ML-SA1 (25 μM) following 30 min pretreatment with DMSO or BafA1 (10 nM). Left: immunofluorescence. Right: quantified pH_i values. Two-way ANOVA with Tukey's test; *p < 0.05; ***p < 0.001.

(D) pH_{lys} in sensor cells expressing mTFP1-hLAMP1-mCherry after treatment with DMSO, EBSS, ML-SA1 (25 μM), or Torin1 (400 nM) for 2 h. Fluorescence ratios were converted to pH_{lys} using a calibration curve (Figure S5B). Mean pH_{lys} ± SD from three experiments (>20 cells each). One-way ANOVA with Dunnett's test; ***p ≤ 0.001.

(E) pH_i measured in sensor cells treated with EBSS, ML-SA1 (25 μM), or Torin1 (400 nM) for 2 h after 30-min pretreatment with DMSO or ML-SI3 (25 μM). Data are mean ± SD; ***p < 0.001 (two-way ANOVA, Tukey's test).

(legend continued on next page)

elevates cytosolic Ca^{2+} in addition to increasing pH_i . Incubation at pH_e 8.5 raised pH_i to 7.8 and elevated cytosolic Ca^{2+} ($\Delta F/F_0 = 0.5$) (Figure 7A). ML-SI3 blocked this Ca^{2+} increase and slightly reduced pH_i under pH_e 7.5 conditions, likely by inhibiting basal TRPML activity. These results suggest that alkaline pH_e triggers lysosomal Ca^{2+} release through TRPML activation.

While low pH_{lys} enhances TRPML1,^{62,63} TRPML3 is stimulated by high pH_{lys} .^{64,65} To assess TRPML3's role in pH_e -induced Ca^{2+} elevation, we silenced TRPML3 and monitored pH_{lys} dynamics. In control cells, alkaline pH_e caused a transient increase in pH_{lys} during the first 30 min, followed by a gradual decrease over 2 h (Figure 7B). In cells treated with ML-SI3 or TRPML3 siRNA, the initial pH_{lys} increase was similar, but pH_{lys} remained elevated thereafter. TRPML3 knockdown also blocked the pH_e -induced cytosolic Ca^{2+} rise (Figure 7C). These data indicate that alkaline pH_e activates TRPML3 via increased pH_{lys} , leading to Ca^{2+} release. This Ca^{2+} likely activates ALG-2, which in turn enhances V-ATPase activity, thereby restoring lysosomal acidity (Figure S6D). While ML-SI3 effectively suppressed starvation-induced pH_i elevation (Figure 5E), it had limited effects on alkaline pH_e -induced pH_i increases (Figure 7A). Because pH_i is influenced by both pH_e and V-ATPase activity and the interplay between pH_i and pH_{lys} remains unclear, it needs to be determined whether pH_e alkalinizes pH_{lys} directly through fluid endocytosis or indirectly via altered pH_i .

To further dissect TRPML3 function, we assessed pH_{lys} in TRPML1-and TRPML3-KO HAP1 cells following serum starvation, ML-SA1, or Torin1 treatment. In wild-type cells, all treatments reduced pH_{lys} (Figures S6E and S6F). This reduction was impaired in TRPML3-KO cells and more so in TRPML1-KO cells. Notably, TRPML1 disruption also reduced TRPML3 expression,⁶⁶ whereas TRPML3 deletion specifically reduced its own expression (Figure S6G). RNF13 and ALG-2 levels were unchanged across genotypes, but ARL8B levels were elevated in both TRPML1-and TRPML3-KO cells (Figure S6H). These findings suggest that TRPML3 is required for proper lysosomal acidification in response to starvation and mTOR inhibition.

As TRPML activation leads to decreased pH_{lys} and elevated pH_i , we next examined how TRPML isoforms affect RNF13 regulation. Depletion of TRPML1 or TRPML3 by siRNA suppressed the EBSS- or ML-SA1-induced increases in pH_i and cytosolic Ca^{2+} (Figures 7D and 7E), with TRPML1 knockdown exerting a stronger effect.

Because ML-SA1 and ML-SI3 affect both TRPML1 and TRPML3, we used the TRPML3-selective agonist SN-2 to isolate TRPML3 function. SN-2 treatment increased cytosolic Ca^{2+} and pH_i (Figure 7F), reduced ARL8B levels, and induced perinuclear lysosome clustering (Figure 7G), supporting a functional role for TRPML3 in lysosomal positioning. To further explore TRPML3's impact on ARL8B, we analyzed ARL8B levels in TRPML1-and TRPML3-KO cells under conditions known to activate TRPML channels. Starvation, alkaline pH_e , and treatment with ML-SA1

or SN-2 decreased ARL8B levels in wild-type cells but not in TRPML1-or TRPML3-KO cells (Figure 7H).

Together, these findings suggest that TRPML3 is essential for RNF13 activation and ARL8B degradation in response to metabolic and environmental cues. We propose a model in which starvation, alkaline pH_e , or ML-SA1 increases pH_i and cytosolic Ca^{2+} , thereby activating RNF13 and promoting ARL8B degradation to drive perinuclear lysosomal positioning (Figure 7I).

Loss of ubiquitin ligase activity in RNF13 L312P is implicated in DEE-73 pathogenesis

Missense variants in *RNF13*, specifically L311S and L312P, have been associated with the neurological disorder DEE-73 in humans.⁵⁰ To elucidate the underlying mechanisms, we analyzed the expression, subcellular localization, and ligase activity of RNF13 L311S and L312P. RNF13 L312P exhibited markedly higher expression than wild-type RNF13, whereas L311S was expressed at levels comparable to the wild type (Figures S7A–S7C). Autoubiquitination activity was substantially reduced in L312P relative to both wild type and L311S (Figure S7B), and only L312P failed to ubiquitinate and degrade ARL8B (Figures S7C–S7E).

To assess whether the 307-EHTPLL-312 motif, resembling a [D/E]xxxL[L/I]-type lysosomal targeting signal, contributes to lysosomal localization, we tested the RNF13 ELL-AAA mutant (E307A, L311A, L312A). This mutant displayed expression and ARL8B degradation activity comparable to the wild type (Figures S7C and S7E). Both L311S and ELL-AAA localized primarily to lysosomes and induced perinuclear lysosomal clustering similarly to wild-type RNF13. In contrast, the ligase-dead CS and L312P mutants failed to cluster lysosomes perinuclearly and showed diminished colocalization with LAMP1, likely due to impaired autoubiquitination (Figure S7F).

To further dissect RNF13 localization determinants, we generated chimeras with RNF128, a PA-TM-RING E3 ligase primarily localized to the endoplasmic reticulum (ER) (Figure S7G). A chimera comprising RNF128's N-terminal luminal and TM domains with RNF13's C-terminal cytosolic region localized to the ER. Conversely, a chimera with RNF13's N-terminal portion fused to RNF128's C-terminal domain recapitulated RNF13's lysosomal localization and colocalized with LAMP1 (Figure S7G). This supports previous findings that the PA domain is a key determinant of endosomal targeting in PA-TM-RING E3 ligases.⁶⁷ These results indicate that the 307-EHTPLL-312 sequence does not function as a lysosomal targeting signal and that lysosomal localization is primarily mediated by RNF13's N-terminal domain.

Collectively, these data suggest that the L312P mutation impairs RNF13 autoubiquitination and E3 ligase activity, thereby disrupting ARL8B degradation and lysosome positioning—mechanisms that likely contribute to DEE-73 pathogenesis in affected individuals. In contrast, the L311S mutation retains ligase activity, indicating that disease mechanisms in these

(F and G) pH_i in sensor cells transfected with siControl or siALG-2 for 72 h, then treated with DMSO, ML-SA1 (25 μM) (F), or Torin1 (400 nM) (G) for 2 h. Mean $\text{pH}_i \pm \text{SD}$ from three replicates. Statistical analysis by two-way ANOVA with Tukey's test; ns, not significant; ** $p < 0.001$.

(H) Model summarizing results shown in this figure.

Created with BioRender.com.

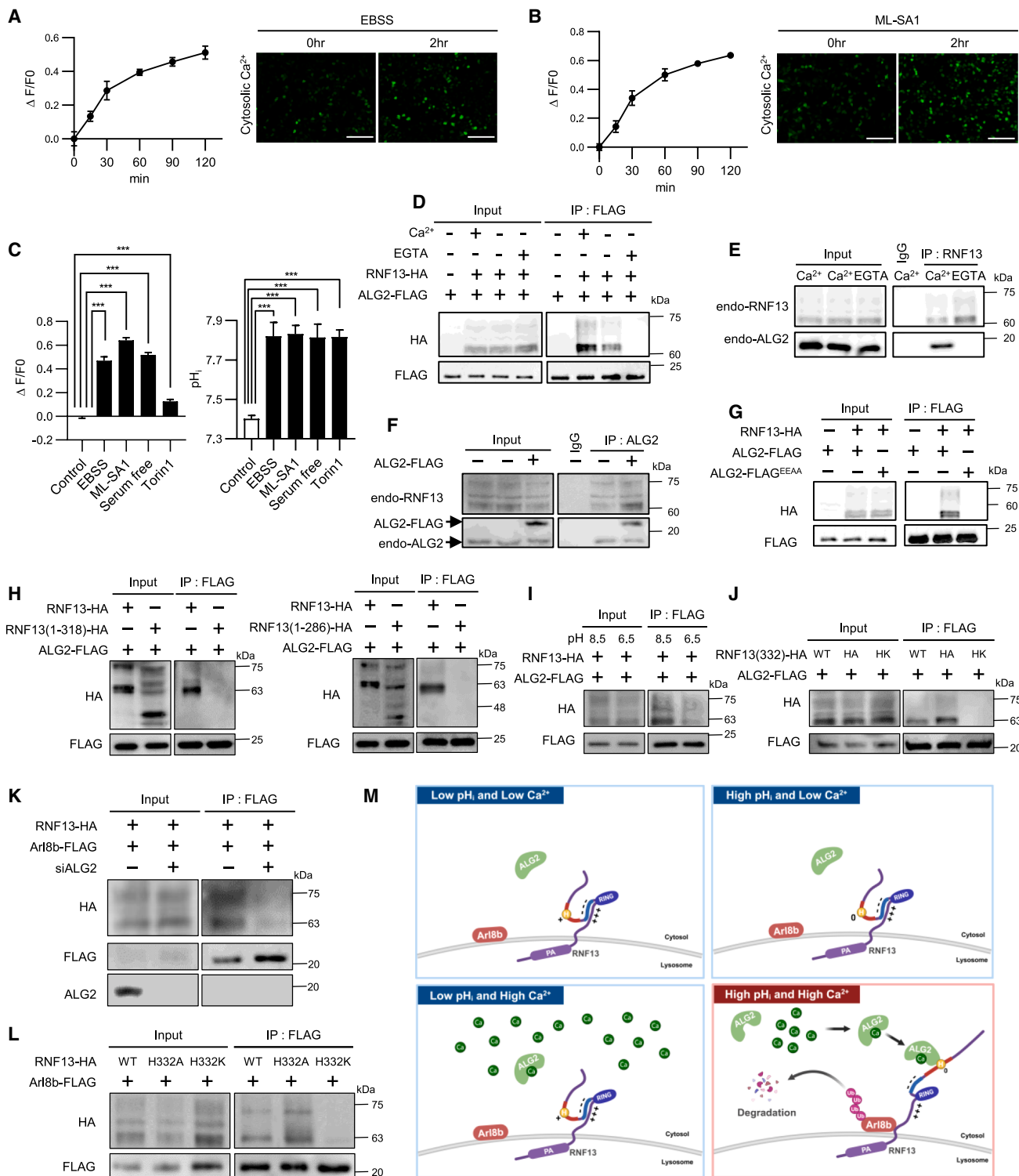


Figure 6. Ca^{2+} -bound ALG-2 activates RNF13 via a His332 deprotonation-dependent interaction with PRR to relieve NRR-mediated repression

(A and B) Cytosolic Ca^{2+} levels in HeLa cells expressing GCaMP6f after 2 h in EBSS (A) or ML-SA1 (25 μM) (B). $\Delta F/F_0$ was normalized to baseline per replicate. Data are mean \pm SD from 3 independent experiments (3 fields each).

(legend continued on next page)

patients may involve distinct or additional pathways, possibly in combination with other genetic factors.

DISCUSSION

ARL8B is a key regulator of lysosomal positioning and function. This study elucidates how alkaline pH_i or nutrient starvation induces ARL8B degradation through RNF13. Our findings support a model in which pH_i and Ca²⁺ modulate RNF13 activity, thereby governing lysosomal distribution in response to environmental changes (Figure 7J).

Regulation of lysosomal positioning by RNF13

RNF13 is a RING-type ubiquitin ligase that transfers ubiquitin from an E2 enzyme to lysine residues on substrates or itself. The activity of RNF13 is regulated by Ca²⁺-bound ALG-2 and the protonation state of H332 in the PRR. Under acidic pH or low Ca²⁺, RNF13 adopts an inactive conformation, with R217 in the NIR domain forming salt bridges with D291 and D293 in the NRR (Figure 2I), thereby blocking ARL8B binding. In contrast, at alkaline pH and elevated Ca²⁺, ALG-2 binds to the PRR where H332 is deprotonated. This binding disrupts the NIR-NRR interaction, freeing R217 to engage ARL8B (Figure 6M). This conformational switch enhances RNF13-mediated ARL8B ubiquitination, promoting lysosomal repositioning toward the perinuclear region. Endogenous RNF13 levels are also affected by H⁺ and Ca²⁺. When inactive, RNF13 may exhibit reduced auto-ubiquitination due to limited E2-Ub access or a lack of available lysine residues. Interestingly, RNF13 mutants lacking the PRR but retaining the NRR show increased auto-degradation and reduced ARL8B degradation. These results suggest that ARL8B interaction with RNF13's substrate-binding site is the main determinant for its ubiquitination, and that RNF13 conformation, controlled by pH_i and Ca²⁺, plays a critical regulatory role.

SKIP, the primary effector of ARL8B, promotes removal of RAB7 from lysosomes via the GTPase-activating protein TBC1D15.⁶⁸ Because ARL8B drives anterograde trafficking and RAB7 mediates retrograde movement through RILP, even modest changes in ARL8B levels could alter the ARL8B:RAB7 ratio on lysosomes, amplifying the effects of RNF13 activity on lysosomal transport. This may explain why small shifts in ARL8B levels produce large changes in positioning.

ALG-2 directly interacts with TRPML1 in a Ca²⁺-dependent manner⁶⁹ and associates with dynamitin independently of Ca²⁺,⁴¹ promoting retrograde lysosomal transport. However, under acidic pH_i, ML-SA1-induced ALG-2 activation does not trigger perinuclear clustering, suggesting the TRPML1-ALG-2-

dynein pathway is pH sensitive. Further work is needed to clarify this regulation.

In cancer, lysosomes often relocate to the periphery, aiding in invasion and metastasis.^{6,70} This redistribution has been observed in bladder,⁸ breast,⁷¹ and prostate cancers.⁷² Acidic tumor pH_e^{73,74} may contribute to peripheral lysosome localization. ARL8B promotes lysosomal protease release in tumors,^{71,72} yet it remains unknown whether RNF13-dependent ARL8B degradation is suppressed in cancer. This potential mechanism and its role in tumor progression deserve further investigation.

Regulation of pH_i by lysosomes

Although pH_i regulation is mainly attributed to plasma membrane transporters,⁷⁵ lysosomes play an underexplored role. Despite occupying only 0.5%–5% of the cell volume, lysosomes maintain an H⁺ concentration 500–1,000 times higher than the cytoplasm via V-ATPase.⁷⁶ Our data indicate lysosomes contribute to starvation-induced cytosolic alkalinization, affecting their positioning. Ca²⁺ efflux via TRPML channels is tightly coupled to V-ATPase-driven H⁺ influx through ALG-2. Prior work showed mTOR inhibition by Torin1 enhances V-ATPase assembly and lysosomal protease activity.⁶⁰ We confirmed that Torin1 lowers pH_{lys} and raises pH_i, dependent on TRPML channel activity and ALG-2. Starvation also increases V-ATPase assembly,⁷⁷ likely through enhanced lysosomal Ca²⁺ release and ALG-2 activation.

Torin1, starvation, and ML-SA1 cause similar pH_i and pH_{lys} shifts, but only starvation and ML-SA1 sufficiently elevate cytosolic Ca²⁺ for lysosome clustering. Although mTOR inhibition can activate TRPML1 and TRPML3,^{78–80} its effects on ALG-2 remain unclear and merit further study.

STAT3 enhances V-ATPase activity and promotes cytoplasmic pH neutralization by translocating to lysosomes under acidic pH.⁸¹ Our findings underscore the lysosome's emerging role in pH_i control. V-ATPase activity is regulated through V1-V0 subcomplex assembly. Proteins affecting lysosomal positioning—like RILP⁸² and TMEM55B⁸³—also influence V-ATPase. PI3P-to-PI4P conversion, triggered by nutrients, dynamically regulates V-ATPase assembly and function.¹⁴ As PI4P functions as a pH sensor,⁸⁴ its protonation may alter effector binding and V-ATPase activity, further impacting lysosomal dynamics. Whether RNF13-mediated ARL8B degradation is integrated into this response remains an open question.

Role of TRPML3 in lysosomal positioning

We identified TRPML3 as a critical mediator of lysosomal Ca²⁺ release during starvation. Although TRPML1 knockdown caused a greater reduction in Ca²⁺ signals, TRPML3 expression was

(C) Left: cytosolic Ca²⁺ levels in Ca²⁺ sensor cells. Right: pH_i in pH_i sensor cells after 2 h with DMSO, EBSS, ML-SA1 (25 μM), serum-free media, or Torin1 (400 nM). Mean ΔF/F₀ and pH_i ± SD were calculated from three replicates. One-way ANOVA with Dunnett's test; ***p < 0.001.

(D–L) CoIP of indicated proteins in HeLa cell lysates: (D) RNF13-HA and ALG-2-FLAG cotransfection; FLAG coIP with or without 100 μM Ca²⁺ or 5 mM EGTA. (E) Endogenous RNF13 and ALG-2 coIP with RNF13 antibodies in the presence of Ca²⁺ or EGTA. (F) CoIP of endogenous RNF13 with ALG-2 antibodies in cells with or without ALG-2-FLAG. (G) RNF13-HA with either ALG-2-FLAG or ALG-2^{E4AA}-FLAG (E47A/E114A mutant); FLAG IP. (H) ALG-2-FLAG with RNF13 (1–318) or RNF13 (1–286); FLAG IP. (I) Cotransfection with ALG-2-FLAG and RNF13-HA; FLAG IP at pH 8.5 or 6.5. (J) ALG-2-FLAG cotransfected with RNF13 H332 mutants; FLAG IP. (K) Cells transfected with siALG-2 or siControl for 48 h, followed by transfection with RNF13-HA and ARL8B-FLAG for 24 h, and coIP with FLAG antibody. (L) Cotransfection with ARL8B-FLAG and RNF13 H332 mutants; FLAG coIP.

(M) Proposed model of RNF13-mediated ARL8B degradation regulated by pH_i and Ca²⁺ levels.

Created with BioRender.com.

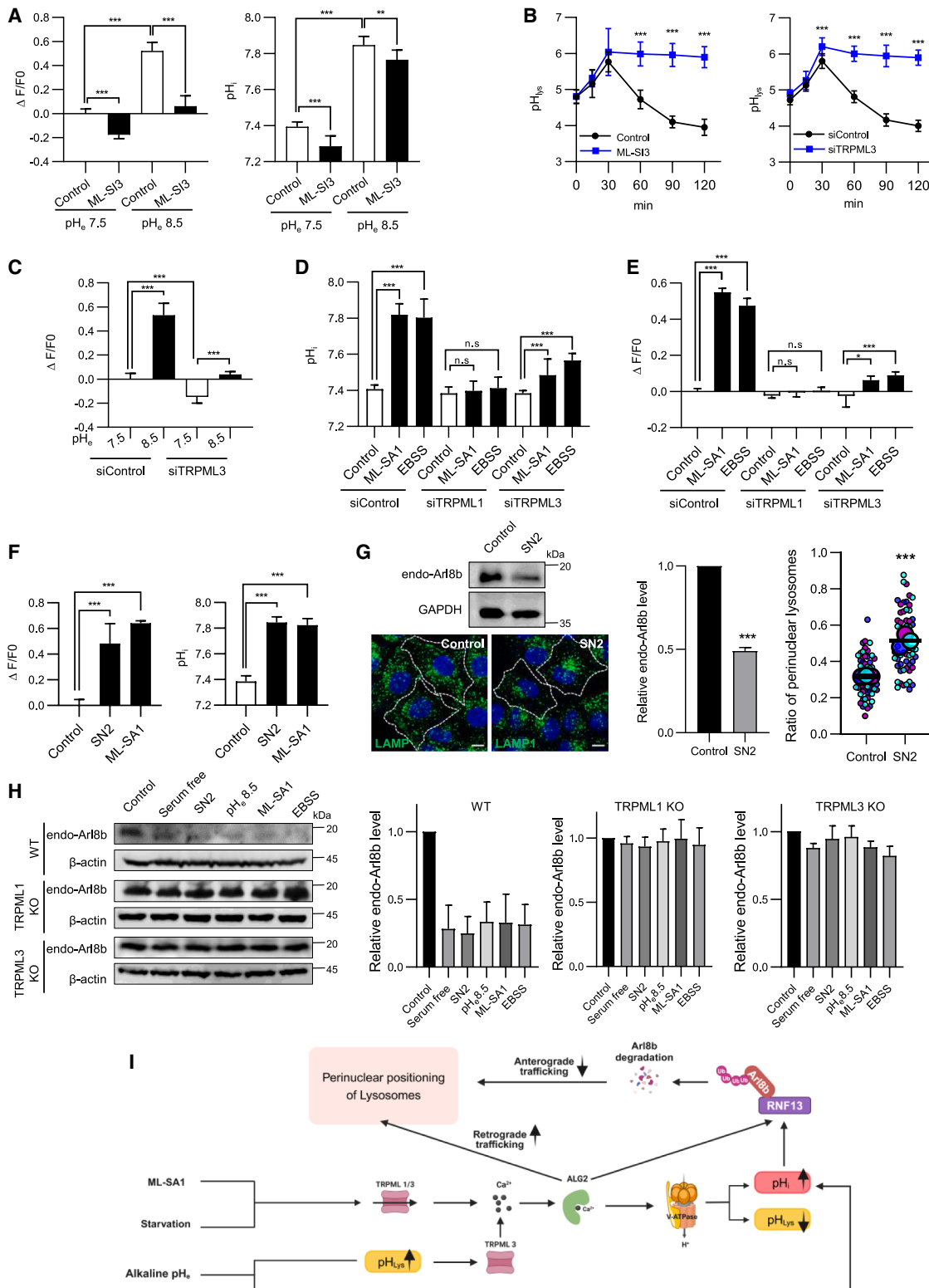


Figure 7. Alkaline pH_e increases cytosolic Ca²⁺ via TRPML3 activation

(A) Ca²⁺ levels (left) and pH_i (right) in sensor cells after 2 h in media at the indicated pH, with or without 30-min pretreatment with ML-SI3 (25 μM). ΔF/F₀ and pH_i values were calculated from three fields per replicate ($n = 3$). Two-way ANOVA with Tukey's test (** $p \leq 0.01$, *** $p \leq 0.001$).

(legend continued on next page)

also reduced in these cells, complicating interpretation. PI3P activates TRPML3 during starvation-induced autophagy,⁶⁶ but whether it also activates TRPML3 on lysosomes under these conditions remains unclear.

Our data show TRPML3 is activated by elevated pH_{lys}.^{64,65} Alkaline pH_e increases pH_{lys}, triggering TRPML3-dependent Ca²⁺ release and ALG-2 activation, which promotes V-ATPase assembly. Agents that raise pH_{lys} (e.g., NH₄Cl, chloroquine, LLOMe) similarly enhance V-ATPase.^{77,88} These results suggest TRPML3 functions as a pH_{lys} sensor that maintains lysosomal acidity by activating V-ATPase in response to elevated pH_{lys}, thus preserving lysosomal homeostasis.

Role of ALG-2 in lysosomal trafficking

ALG-2 not only activates RNF13 but also plays a central role in starvation-induced perinuclear lysosomal clustering via V-ATPase activation, TRPML1 binding, and dynein-dynactin recruitment. Although thapsigargin raises cytosolic Ca²⁺, it does not affect pH_i and alone fails to activate ALG-2 sufficiently. ALG-2 recruitment to lysosomes is thought to require TRPML1-mediated local Ca²⁺ release.⁴¹ While TRPML1 has been implicated in local signaling during autophagy⁴⁶ and lysosome movement,⁸⁶ our findings suggest its activation induces a global Ca²⁺ increase, consistent with recent studies.⁸⁷⁻⁸⁹ The combined use of thapsigargin and Torin1 activates RNF13, indicating that mTOR inhibition may sensitize ALG-2 to global Ca²⁺ rises. Future studies are needed to dissect how ALG-2 responds to spatial dynamics of Ca²⁺ signaling.

RNF13 dysfunction in DEE-73

The RNF13 L312P variant exhibits impaired auto- and ARL8B ubiquitination. In contrast, the L312A mutation in the RNF13 ELL-AAA mutant retains wild-type activity, suggesting that the proline-induced structural kink may disrupt access of ALG-2 to the PRR or E2 to the RING domain. A DEE-73-associated nonsense variant (Glu301X)⁴⁹ lacking the PRR is expected not to ubiquitinate ARL8B, similar to RNF13 (1–305). Since ARL8B regulates axon branching and density during brain development,²⁶ these RNF13 variants likely contribute to DEE-73 by failing to modulate ARL8B levels.

Conclusions

This study reveals how RNF13 integrates pH_i and Ca²⁺ signals to regulate lysosomal transport via ARL8B degradation. These

findings expand our understanding of lysosomal regulation by environmental cues. While ARL8B-SKIP interaction is a key mechanism in anterograde lysosomal transport, other ARL8B effectors^{28,31-33} remain incompletely characterized. Further investigation is needed to determine how RNF13 influences these pathways during lysosomal repositioning and autophagy.

Limitations of the study

This study has several limitations. We did not address the heterogeneity of lysosomes or cytoplasmic subregions. Our pH_i measurements reflect average cytosolic values and may not capture local pH fluctuations near lysosomes. Such localized pH, likely shaped by V-ATPase activity and lysosomal Ca²⁺ release, may influence membrane-associated signaling pathways. For example, mTORC1 activity differs between perinuclear and peripheral lysosomes,⁴⁵ potentially due to spatial variations in local pH. Future studies with organelle- and region-specific pH and Ca²⁺ sensors could provide more refined insights into lysosome positioning and function.

RESOURCE AVAILABILITY

Lead contact

Requests for further information and resources should be directed to and will be fulfilled by the lead contact, Jong-Bok Yoon (yoonj@yonsei.ac.kr).

Material availability

Plasmids and cell lines generated in this study are available from the [lead contact](#) upon request.

Data and code availability

- Original western blot images and microscopy data have been deposited at Mendeley and are publicly available as of the date of publication. The DOI is listed in the [key resources table](#).
- This paper does not report original code.
- Any additional information required to reanalyze the data reported in this paper is available from the [lead contact](#) upon request.

ACKNOWLEDGMENTS

This work was supported by grants from the National Research Foundation of Korea (NRF-2021R1A2C1011189) and Ministry of Science and ICT (RS-2023-00273665) by the Korean government. We thank Young Jin Yoon from the Research & Technology Support Team, Songeui Medical Campus, The Catholic University of Korea, for technical assistance.

(B) Left: pH_{lys} in sensor cells pretreated with DMSO or ML-SI3 (25 μM, 30 min) and incubated in pH 8.5 media with DMSO or ML-SI3 for 2 h. Right: pH_{lys} in cells transfected with control or TRPML3 siRNA for 72 h, followed by 2 h incubation in pH 8.5 media. Data were quantified from 18 to 35 cells per condition in three experiments. ***p < 0.001, unpaired two-tailed t test.

(C) Ca²⁺ levels in sensor cells transfected with control or TRPML3 siRNA, followed by 2 h incubation in media at pH 7.5 or 8.5. ΔF/F₀ was measured in 3 fields per condition; mean ± SD calculated from 3 replicates. Two-way ANOVA with Tukey's test: ***p < 0.001.

(D and E) pH_i (D) and Ca²⁺ levels (E) in sensor cells transfected with indicated siRNAs for 72 h, followed by 2 h treatment with DMSO, ML-SA1 (25 μM), or EBSS. Data are mean ± SD (n = 3). Two-way ANOVA with Tukey's test (ns, not significant; *p < 0.05; ***p < 0.001).

(F) Ca²⁺ and pH_i in sensor cells after 2 h with DMSO, SN-2 (30 μM), or ML-SA1 (25 μM). One-way ANOVA with Dunnett's test (**p < 0.001).

(G) Western blot of endogenous ARL8B and LAMP1 immunofluorescence in HeLa cells treated with DMSO or SN-2 for 2 h. ARL8B levels normalized to β-actin (mean ± SD, n = 3). Right: SuperPlot of perinuclear/total LAMP1 ratio from three experiments. ***p < 0.001, unpaired two-tailed t test.

(H) Western blot and quantification of endogenous ARL8B in HAP1 WT, TRPML1 KO, and TRPML3 KO cells treated as indicated for 2 h. Data are mean ± SD (n = 3).

(I) Model: starvation, alkaline pH_e, or ML-SA1 increases pH_i and Ca²⁺, activating RNF13 to degrade ARL8B and promote perinuclear lysosome accumulation. Created with [BioRender.com](https://biorender.com).

AUTHOR CONTRIBUTIONS

Formal analysis, L.T.T., A.V.V., and Y.H.; investigation, L.T.T., A.V.V., S.S., C.L., S.-H.P., and E.-B.C.; resources and discussion, Y.H. and H.J.K.; methodology, L.T.T. and J.-B.Y.; conceptualization, S.K. and J.-B.Y.; supervision, S.K. and J.-B.Y.; writing – review and editing, S.K. and J.-B.Y.; and funding acquisition, S.K. and J.-B.Y.

DECLARATION OF INTERESTS

The authors declare no conflict of interest.

STAR METHODS

Detailed methods are provided in the online version of this paper and include the following:

- KEY RESOURCES TABLE
- EXPERIMENTAL MODEL AND STUDY PARTICIPANT DETAILS
 - Cell culture
- METHOD DETAILS
 - Plasmids
 - RNAi
 - RNA extraction and quantitative real-time PCR (qRT-PCR)
 - Cell line generation
 - Cell transfection and treatment
 - Identification of ARL8B as a potential RNF13 substrate using proximity-dependent biotin labeling
 - Co-immunoprecipitation and western blot analysis
 - Ubiquitination assay
 - Immunofluorescence microscopy
 - Time-lapse confocal imaging
 - Analysis of intracellular distribution of lysosomes
 - Measurement of pH_i and pH_{lys}
 - Measurement of lysosomal pH using lysosensor staining
 - Measurement of cytoplasmic Ca²⁺ levels
 - Molecular docking and refinement
- QUANTIFICATION AND STATISTICAL ANALYSIS

SUPPLEMENTAL INFORMATION

Supplemental information can be found online at <https://doi.org/10.1016/j.celrep.2025.116053>.

Received: June 20, 2024

Revised: May 21, 2025

Accepted: July 4, 2025

Published: July 24, 2025

REFERENCES

1. Ballabio, A., and Bonifacino, J.S. (2020). Lysosomes as dynamic regulators of cell and organismal homeostasis. *Nat. Rev. Mol. Cell Biol.* 21, 101–118. <https://doi.org/10.1038/s41580-019-0185-4>.
2. Saftig, P., and Puertollano, R. (2021). How Lysosomes Sense, Integrate, and Cope with Stress. *Trends Biochem. Sci.* 46, 97–112. <https://doi.org/10.1016/j.tibs.2020.09.004>.
3. Lim, C.Y., and Zoncu, R. (2016). The lysosome as a command-and-control center for cellular metabolism. *J. Cell Biol.* 214, 653–664. <https://doi.org/10.1083/jcb.201607005>.
4. Cabukusta, B., and Neefjes, J. (2018). Mechanisms of lysosomal positioning and movement. *Traffic* 19, 761–769. <https://doi.org/10.1111/tra.12587>.
5. Bonifacino, J.S., and Neefjes, J. (2017). Moving and positioning the endolysosomal system. *Curr. Opin. Cell Biol.* 47, 1–8. <https://doi.org/10.1016/j.ceb.2017.01.008>.
6. Pu, J., Guardia, C.M., Keren-Kaplan, T., and Bonifacino, J.S. (2016). Mechanisms and functions of lysosome positioning. *J. Cell Sci.* 129, 4329–4339. <https://doi.org/10.1242/jcs.196287>.
7. Raiborg, C., Wenzel, E.M., Pedersen, N.M., Olsvik, H., Schink, K.O., Schultz, S.W., Vietri, M., Nisi, V., Bucci, C., Brech, A., et al. (2015). Repeated ER-endosome contacts promote endosome translocation and neurite outgrowth. *Nature* 520, 234–238. <https://doi.org/10.1038/nature14359>.
8. Mathur, P., De Barros Santos, C., Lachuer, H., Patat, J., Latgé, B., Radvanyi, F., Goud, B., and Schauer, K. (2023). Transcription factor EB regulates phosphatidylinositol-3-phosphate levels that control lysosome positioning in the bladder cancer model. *Commun. Biol.* 6, 114. <https://doi.org/10.1038/s42003-023-04501-1>.
9. Starling, G.P., Yip, Y.Y., Sanger, A., Morton, P.E., Eden, E.R., and Dodding, M.P. (2016). Folliculin directs the formation of a Rab34-RILP complex to control the nutrient-dependent dynamic distribution of lysosomes. *EMBO Rep.* 17, 823–841. <https://doi.org/10.1525/embr.201541382>.
10. Byfield, M.P., Murray, J.T., and Backer, J.M. (2005). hVps34 is a nutrient-regulated lipid kinase required for activation of p70 S6 kinase. *J. Biol. Chem.* 280, 33076–33082. <https://doi.org/10.1074/jbc.M507201200>.
11. Nobukuni, T., Joaquin, M., Roccio, M., Dann, S.G., Kim, S.Y., Gulati, P., Byfield, M.P., Backer, J.M., Natt, F., Bos, J.L., et al. (2005). Amino acids mediate mTOR/raptor signaling through activation of class 3 phosphatidylinositol 3OH-kinase. *Proc. Natl. Acad. Sci. USA* 102, 14238–14243. <https://doi.org/10.1073/pnas.0506925102>.
12. Marat, A.L., Wallroth, A., Lo, W.T., Müller, R., Norata, G.D., Falasca, M., Schultz, C., and Haucke, V. (2017). mTORC1 activity repression by late endosomal phosphatidylinositol 3,4-bisphosphate. *Science* 356, 968–972. <https://doi.org/10.1126/science.aaf8310>.
13. Dong, X.-p., Shen, D., Wang, X., Dawson, T., Li, X., Zhang, Q., Cheng, X., Zhang, Y., Weisman, L.S., Delling, M., and Xu, H. (2010). PI(3,5)P2 controls membrane trafficking by direct activation of mucolipin Ca²⁺ release channels in the endolysosome. *Nat. Commun.* 1, 38. <https://doi.org/10.1038/ncomms1037>.
14. Ebner, M., Puchkov, D., López-Ortega, O., Muthukottiappan, P., Su, Y., Schmied, C., Zillmann, S., Nikonenko, I., Koddebusch, J., Dornan, G.L., et al. (2023). Nutrient-regulated control of lysosome function by signaling lipid conversion. *Cell* 186, 5328–5346. <https://doi.org/10.1016/j.cell.2023.09.027>.
15. Rocha, N., Kuijil, C., van der Kant, R., Janssen, L., Houben, D., Janssen, H., Zwart, W., and Neefjes, J. (2009). Cholesterol sensor ORP1L contacts the ER protein VAP to control Rab7-RILP-p150Glued and late endosome positioning. *J. Cell Biol.* 185, 1209–1225. <https://doi.org/10.1083/jcb.200811005>.
16. Rezaul, K., Gupta, D., Semenova, I., Ikeda, K., Kraikivski, P., Yu, J., Cowan, A., Zaliapin, I., and Rodionov, V. (2016). Engineered Tug-of-War Between Kinesin and Dynein Controls Direction of Microtubule Based Transport In Vivo. *Traffic* 17, 475–486. <https://doi.org/10.1111/tra.12385>.
17. Johansson, M., Rocha, N., Zwart, W., Jordens, I., Janssen, L., Kuijil, C., Olkkonen, V.M., and Neefjes, J. (2007). Activation of endosomal dynein motors by stepwise assembly of Rab7-RILP-p150Glued, ORP1L, and the receptor betall spectrin. *J. Cell Biol.* 176, 459–471. <https://doi.org/10.1083/jcb.200606077>.
18. Jin, R.U., and Mills, J.C. (2014). RAB26 coordinates lysosome traffic and mitochondrial localization. *J. Cell Sci.* 127, 1018–1032. <https://doi.org/10.1242/jcs.138776>.
19. Zhou, Y., Liu, Z., Zhang, S., Zhuang, R., Liu, H., Liu, X., Qiu, X., Zhang, M., Zheng, Y., Li, L., et al. (2020). RILP Restricts Insulin Secretion Through Mediating Lysosomal Degradation of Proinsulin. *Diabetes*. 69, 67–82. <https://doi.org/10.2337/db19-0086>.
20. Wang, T., and Hong, W. (2002). Interorganellar regulation of lysosome positioning by the Golgi apparatus through Rab34 interaction with Rab-interacting lysosomal protein. *Mol. Biol. Cell* 13, 4317–4332. <https://doi.org/10.1091/mbc.e02-05-0280>.

21. Goldenberg, N.M., Grinstein, S., and Silverman, M. (2007). Golgi-bound Rab34 is a novel member of the secretory pathway. *Mol. Biol. Cell* 18, 4762–4771. <https://doi.org/10.1091/mbc.e06-11-0991>.
22. Chen, L., Hu, J., Yun, Y., and Wang, T. (2010). Rab36 regulates the spatial distribution of late endosomes and lysosomes through a similar mechanism to Rab34. *Mol. Membr. Biol.* 27, 23–30. <https://doi.org/10.3109/09687680903417470>.
23. Garg, S., Sharma, M., Ung, C., Tuli, A., Barral, D.C., Hava, D.L., Veerapen, N., Besra, G.S., Hacohen, N., and Brenner, M.B. (2011). Lysosomal trafficking, antigen presentation, and microbial killing are controlled by the Arf-like GTPase Arl8b. *Immunity* 35, 182–193. <https://doi.org/10.1016/j.immuni.2011.06.009>.
24. Khatter, D., Raina, V.B., Dwivedi, D., Sindhwan, A., Bahl, S., and Sharma, M. (2015). The small GTPase Arl8b regulates assembly of the mammalian HOPS complex on lysosomes. *J. Cell Sci.* 128, 1746–1761. <https://doi.org/10.1242/jcs.162651>.
25. Sindhwan, A., Arya, S.B., Kaur, H., Jagga, D., Tuli, A., and Sharma, M. (2017). *Salmonella* exploits the host endolysosomal tethering factor HOPS complex to promote its intravacuolar replication. *PLoS Pathog.* 13, e1006700. <https://doi.org/10.1371/journal.ppat.1006700>.
26. Adnan, G., Rubikaite, A., Khan, M., Reber, M., Sutterlin, P., Hindges, R., and Drescher, U. (2020). The GTPase Arl8B Plays a Principle Role in the Positioning of Interstitial Axon Branches by Spatially Controlling Autophagosome and Lysosome Location. *J. Neurosci.* 40, 8103–8118. <https://doi.org/10.1523/jneurosci.1759-19.2020>.
27. Ghosh, S., Dellibovi-Ragheb, T.A., Kerviel, A., Pak, E., Qiu, Q., Fisher, M., Takvorian, P.M., Bleck, C., Hsu, V.W., Fehr, A.R., et al. (2020). β -Coronaviruses Use Lysosomes for Egress Instead of the Biosynthetic Secretory Pathway. *Cell* 183, 1520–1535. <https://doi.org/10.1016/j.cell.2020.10.039>.
28. Marwaha, R., Arya, S.B., Jagga, D., Kaur, H., Tuli, A., and Sharma, M. (2017). The Rab7 effector PLEKHM1 binds Arl8b to promote cargo traffic to lysosomes. *J. Cell Biol.* 216, 1051–1070. <https://doi.org/10.1083/jcb.201607085>.
29. Rosa-Ferreira, C., and Munro, S. (2011). Arl8 and SKIP act together to link lysosomes to kinesin-1. *Dev. Cell* 21, 1171–1178. <https://doi.org/10.1016/j.devcel.2011.10.007>.
30. Pu, J., Schindler, C., Jia, R., Jarnik, M., Backlund, P., and Bonifacino, J.S. (2015). BORC, a multisubunit complex that regulates lysosome positioning. *Dev. Cell* 33, 176–188. <https://doi.org/10.1016/j.devcel.2015.02.011>.
31. Keren-Kaplan, T., Sarić, A., Ghosh, S., Williamson, C.D., Jia, R., Li, Y., and Bonifacino, J.S. (2022). RUFY3 and RUFY4 are ARL8 effectors that promote coupling of endolysosomes to dynein-dynactin. *Nat. Commun.* 13, 1506. <https://doi.org/10.1038/s41467-022-28952-y>.
32. Kumar, G., Chawla, P., Dhiman, N., Chadha, S., Sharma, S., Sethi, K., Sharma, M., and Tuli, A. (2022). RUFY3 links Arl8b and JIP4-Dynein complex to regulate lysosome size and positioning. *Nat. Commun.* 13, 1540. <https://doi.org/10.1038/s41467-022-29077-y>.
33. Kumar, R., Khan, M., Francis, V., Aguilera, A., Kulasekaran, G., Banks, E., and McPherson, P.S. (2024). DENND6A links Arl8b to a Rab34/RILP/dynein complex, regulating lysosomal positioning and autophagy. *Nat. Commun.* 15, 919. <https://doi.org/10.1038/s41467-024-44957-1>.
34. Johnson, D.E., Ostrowski, P., Jaumouillé, V., and Grinstein, S. (2016). The position of lysosomes within the cell determines their luminal pH. *J. Cell Biol.* 212, 677–692. <https://doi.org/10.1083/jcb.201507112>.
35. Fellenz, M.P., and Gerweck, L.E. (1988). Influence of extracellular pH on intracellular pH and cell energy status: relationship to hyperthermic sensitivity. *Radiat. Res.* 116, 305–312.
36. Mizuno, S., Demura, Y., Ameshima, S., Okamura, S., Miyamori, I., and Ishizaki, T. (2002). Alkalosis stimulates endothelial nitric oxide synthase in cultured human pulmonary arterial endothelial cells. *Am. J. Physiol. Lung Cell. Mol. Physiol.* 283, L113–L119. <https://doi.org/10.1152/ajplung.00436.2001>.
37. Xu, T., Su, H., Ganapathy, S., and Yuan, Z.M. (2011). Modulation of autophagic activity by extracellular pH. *Autophagy* 7, 1316–1322. <https://doi.org/10.4161/auto.7.11.17785>.
38. Heuser, J. (1989). Changes in lysosome shape and distribution correlated with changes in cytoplasmic pH. *J. Cell Biol.* 108, 855–864. <https://doi.org/10.1083/jcb.108.3.855>.
39. Parton, R.G., Dotti, C.G., Bacallao, R., Kurtz, I., Simons, K., and Prydz, K. (1991). pH-induced microtubule-dependent redistribution of late endosomes in neuronal and epithelial cells. *J. Cell Biol.* 113, 261–274. <https://doi.org/10.1083/jcb.113.2.261>.
40. Jia, R., and Bonifacino, J.S. (2019). Lysosome Positioning Influences mTORC2 and AKT Signaling. *Mol. Cell* 75, 26–38. <https://doi.org/10.1016/j.molcel.2019.05.009>.
41. Li, X., Rydzewski, N., Hider, A., Zhang, X., Yang, J., Wang, W., Gao, Q., Cheng, X., and Xu, H. (2016). A molecular mechanism to regulate lysosome motility for lysosome positioning and tubulation. *Nat. Cell Biol.* 18, 404–417. <https://doi.org/10.1038/ncb3324>.
42. Willett, R., Martina, J.A., Zewe, J.P., Wills, R., Hammond, G.R.V., and Puertollano, R. (2017). TFEB regulates lysosomal positioning by modulating TMEM55B expression and JIP4 recruitment to lysosomes. *Nat. Commun.* 8, 1580. <https://doi.org/10.1038/s41467-017-01871-z>.
43. Filipek, P.A., de Araujo, M.E.G., Vogel, G.F., De Smet, C.H., Eberharter, D., Rebsamen, M., Rudashevskaya, E.L., Kremser, L., Yordanov, T., Tschaikner, P., et al. (2017). LAMTOR/Ragulator is a negative regulator of Arl8b- and BORC-dependent late endosomal positioning. *J. Cell Biol.* 216, 4199–4215. <https://doi.org/10.1083/jcb.201703061>.
44. Pu, J., Keren-Kaplan, T., and Bonifacino, J.S. (2017). A Ragulator-BORC interaction controls lysosome positioning in response to amino acid availability. *J. Cell Biol.* 216, 4183–4197. <https://doi.org/10.1083/jcb.201703094>.
45. Korolchuk, V.I., Saiki, S., Lichtenberg, M., Siddiqi, F.H., Roberts, E.A., Imarisio, S., Jahreiss, L., Sarkar, S., Futter, M., Menzies, F.M., et al. (2011). Lysosomal positioning coordinates cellular nutrient responses. *Nat. Cell Biol.* 13, 453–460. <https://doi.org/10.1038/ncb2204>.
46. Scotto Rosato, A., Montefusco, S., Soldati, C., Di Paola, S., Capuozzo, A., Monfregola, J., Polishchuk, E., Amabile, A., Grimm, C., Lombardo, A., et al. (2019). TRPML1 links lysosomal calcium to autophagosome biogenesis through the activation of the CaMKK β /VPS34 pathway. *Nat. Commun.* 10, 5630. <https://doi.org/10.1038/s41467-019-13572-w>.
47. Medina, D.L., Di Paola, S., Peluso, I., Armani, A., De Stefani, D., Venditti, R., Montefusco, S., Scotto-Rosato, A., Prezioso, C., Forrester, A., et al. (2015). Lysosomal calcium signalling regulates autophagy through calcineurin and TFEB. *Nat. Cell Biol.* 17, 288–299. <https://doi.org/10.1038/ncb3114>.
48. Cabana, V.C., and Lussier, M.P. (2022). From Drosophila to Human: Biological Function of E3 Ligase Godzilla and Its Role in Disease. *Cells* 11, 380. <https://doi.org/10.3390/cells11030380>.
49. Jin, X., Cheng, H., Chen, J., and Zhu, D. (2011). RNF13: an emerging RING finger ubiquitin ligase important in cell proliferation. *FEBS J.* 278, 78–84. <https://doi.org/10.1111/j.1742-4658.2010.07925.x>.
50. Edvardson, S., Nicolae, C.M., Noh, G.J., Burton, J.E., Punzi, G., Shaag, A., Bischetsrieder, J., De Grassi, A., Pierri, C.L., Elpeleg, O., and Moldovan, G. L. (2019). Heterozygous RNF13 Gain-of-Function Variants Are Associated with Congenital Microcephaly, Epileptic Encephalopathy, Blindness, and Failure to Thrive. *Am. J. Hum. Genet.* 104, 179–185. <https://doi.org/10.1016/j.ajhg.2018.11.018>.
51. Cabana, V.C., Bouchard, A.Y., Sénecal, A.M., Ghilarducci, K., Kourrich, S., Cappadocia, L., and Lussier, M.P. (2021). RNF13 Dileucine Motif Variants L311S and L312P Interfere with Endosomal Localization and AP-3 Complex Association. *Cells* 10, 3063. <https://doi.org/10.3390/cells10113063>.

52. Deshar, R., Yoo, W., Cho, E.B., Kim, S., and Yoon, J.B. (2019). RNF8 mediates NONO degradation following UV-induced DNA damage to properly terminate ATR-CHK1 checkpoint signaling. *Nucleic Acids Res.* 47, 762–778. <https://doi.org/10.1093/nar/gky1166>.
53. Yoo, W., Cho, E.B., Kim, S., and Yoon, J.B. (2019). The E3 ubiquitin ligase MARC3 regulates ERGIC3-dependent trafficking of secretory proteins. *J. Biol. Chem.* 294, 10900–10912. <https://doi.org/10.1074/jbc.RA119.007435>.
54. Deshar, R., Moon, S., Yoo, W., Cho, E.B., Yoon, S.K., and Yoon, J.B. (2016). RNF167 targets Arl8B for degradation to regulate lysosome positioning and endocytic trafficking. *FEBS J.* 283, 4583–4599. <https://doi.org/10.1111/febs.13947>.
55. Oltion, K., Carelli, J.D., Yang, T., See, S.K., Wang, H.Y., Kampmann, M., and Taunton, J. (2023). An E3 ligase network engages GCN1 to promote the degradation of translation factors on stalled ribosomes. *Cell* 186, 346–362. <https://doi.org/10.1016/j.cell.2022.12.025>.
56. Jumper, J., Evans, R., Pritzel, A., Green, T., Figurnov, M., Ronneberger, O., Tunyasuvunakool, K., Bates, R., Žídek, A., Potapenko, A., et al. (2021). Highly accurate protein structure prediction with AlphaFold. *Nature* 596, 583–589. <https://doi.org/10.1038/s41586-021-03819-2>.
57. Koivusalo, M., Welch, C., Hayashi, H., Scott, C.C., Kim, M., Alexander, T., Touret, N., Hahn, K.M., and Grinstein, S. (2010). Amiloride inhibits macro-pinocytosis by lowering submembranous pH and preventing Rac1 and Cdc42 signaling. *J. Cell Biol.* 188, 547–563. <https://doi.org/10.1083/jcb.200908086>.
58. Sankaranarayanan, S., De Angelis, D., Rothman, J.E., and Ryan, T.A. (2000). The use of pHluorins for optical measurements of presynaptic activity. *Biophys. J.* 79, 2199–2208. [https://doi.org/10.1016/s0006-3495\(00\)76468-x](https://doi.org/10.1016/s0006-3495(00)76468-x).
59. Chin, M.Y., Patwardhan, A.R., Ang, K.H., Wang, A.L., Alquezar, C., Welch, M., Nguyen, P.T., Grabe, M., Molofsky, A.V., Arkin, M.R., and Kao, A.W. (2021). Genetically Encoded, pH-Sensitive mTFP1 Biosensor for Probing Lysosomal pH. *ACS Sens.* 6, 2168–2180. <https://doi.org/10.1021/acssensors.0c02318>.
60. Ratto, E., Chowdhury, S.R., Siefert, N.S., Schneider, M., Wittmann, M., Helm, D., and Palm, W. (2022). Direct control of lysosomal catabolic activity by mTORC1 through regulation of V-ATPase assembly. *Nat. Commun.* 13, 4848. <https://doi.org/10.1038/s41467-022-32515-6>.
61. Werley, C.A., Boccardo, S., Rigamonti, A., Hansson, E.M., and Cohen, A. E. (2020). Multiplexed Optical Sensors in Arrayed Islands of Cells for multimodal recordings of cellular physiology. *Nat. Commun.* 11, 3881. <https://doi.org/10.1038/s41467-020-17607-5>.
62. Xu, H., Delling, M., Li, L., Dong, X., and Clapham, D.E. (2007). Activating mutation in a mucolipin transient receptor potential channel leads to melanocyte loss in varitint-waddler mice. *Proc. Natl. Acad. Sci. USA* 104, 18321–18326. <https://doi.org/10.1073/pnas.0709096104>.
63. Li, M., Zhang, W.K., Benvin, N.M., Zhou, X., Su, D., Li, H., Wang, S., Michailidis, I.E., Tong, L., Li, X., and Yang, J. (2017). Structural basis of dual Ca(2+)/pH regulation of the endolysosomal TRPML1 channel. *Nat. Struct. Mol. Biol.* 24, 205–213. <https://doi.org/10.1038/nsmb.3362>.
64. Kim, H.J., Li, Q., Tjon-Kon-Sang, S., So, I., Kiselyov, K., Soyombo, A.A., and Muallem, S. (2008). A novel mode of TRPML3 regulation by extracellular pH absent in the varitint-waddler phenotype. *Embo J.* 27, 1197–1205. <https://doi.org/10.1038/emboj.2008.56>.
65. Zhou, X., Li, M., Su, D., Jia, Q., Li, H., Li, X., and Yang, J. (2017). Cryo-EM structures of the human endolysosomal TRPML3 channel in three distinct states. *Nat. Struct. Mol. Biol.* 24, 1146–1154. <https://doi.org/10.1038/nsmb.3502>.
66. Kim, S.W., Kim, M.K., Hong, S., Choi, A., Choi, J.H., Muallem, S., So, I., Yang, D., and Kim, H.J. (2022). The intracellular Ca(2+) channel TRPML3 is a PI3P effector that regulates autophagosome biogenesis. *Proc. Natl. Acad. Sci. USA* 119, e2200085119. <https://doi.org/10.1073/pnas.2200085119>.
67. van Dijk, J.R., Yamazaki, Y., and Palmer, R.H. (2014). Tumour-associated mutations of PA-TM-RING ubiquitin ligases RNF167/RNF13 identify the PA domain as a determinant for endosomal localization. *Biochem. J.* 459, 27–36. <https://doi.org/10.1042/bj20131067>.
68. Jongsma, M.L., Bakker, J., Cabukusta, B., Liv, N., van Elsland, D., Fermie, J., Akkermans, J.L., Kuijl, C., van der Zanden, S.Y., Janssen, L., et al. (2020). SKIP-HOPS recruits TBC1D15 for a Rab7-to-Arl8b identity switch to control late endosome transport. *Embo J.* 39, e102301. <https://doi.org/10.1525/embj.2019102301>.
69. Vergara-Jauregui, S., Martina, J.A., and Puertollano, R. (2009). Identification of the penta-EF-hand protein ALG-2 as a Ca2+-dependent interactor of mucolipin-1. *J. Biol. Chem.* 284, 36357–36366. <https://doi.org/10.1074/jbc.M109.047241>.
70. Kallunki, T., Olsen, O.D., and Jäättelä, M. (2013). Cancer-associated lysosomal changes: friends or foes? *Oncogene* 32, 1995–2004. <https://doi.org/10.1038/onc.2012.292>.
71. Wu, P.-H., Onodera, Y., Giaccia, A.J., Le, Q.-T., Shimizu, S., Shirato, H., and Nam, J.-M. (2020). Lysosomal trafficking mediated by Arl8b and BORG promotes invasion of cancer cells that survive radiation. *Commun. Biol.* 3, 620. <https://doi.org/10.1038/s42003-020-01339-9>.
72. Dykes, S.S., Gray, A.L., Coleman, D.T., Saxena, M., Stephens, C.A., Carroll, J.L., Pruitt, K., and Cardelli, J.A. (2016). The Arf-like GTPase Arl8b is essential for three-dimensional invasive growth of prostate cancer in vitro and xenograft formation and growth in vivo. *Oncotarget* 7, 31037–31052. <https://doi.org/10.18632/oncotarget.8832>.
73. Glunde, K., Guggino, S.E., Solaiyappan, M., Pathak, A.P., Ichikawa, Y., and Bhujwalla, Z.M. (2003). Extracellular acidification alters lysosomal trafficking in human breast cancer cells. *Neoplasia* 5, 533–545. [https://doi.org/10.1016/s1476-5586\(03\)80037-4](https://doi.org/10.1016/s1476-5586(03)80037-4).
74. Ji, K., Mayernik, L., Moin, K., and Sloane, B.F. (2019). Acidosis and proteolysis in the tumor microenvironment. *Cancer Metastasis Rev.* 38, 103–112. <https://doi.org/10.1007/s10555-019-09796-3>.
75. Casey, J.R., Grinstein, S., and Orlowski, J. (2010). Sensors and regulators of intracellular pH. *Nat. Rev. Mol. Cell Biol.* 11, 50–61. <https://doi.org/10.1038/nrm2820>.
76. Mindell, J.A. (2012). Lysosomal acidification mechanisms. *Annu. Rev. Physiol.* 74, 69–86. <https://doi.org/10.1146/annurev-physiol-012110-142317>.
77. Stransky, L.A., and Forgac, M. (2015). Amino Acid Availability Modulates Vacuolar H+-ATPase Assembly. *J. Biol. Chem.* 290, 27360–27369. <https://doi.org/10.1074/jbc.M115.659128>.
78. Onyenwoke, R.U., Sexton, J.Z., Yan, F., Díaz, M.C.H., Forsberg, L.J., Major, M.B., and Brenman, J.E. (2015). The mucolipidosis IV Ca2+ channel TRPML1 (MCOLN1) is regulated by the TOR kinase. *Biochem. J.* 470, 331–342. <https://doi.org/10.1042/bj20150219>.
79. Sun, X., Yang, Y., Zhong, X.Z., Cao, Q., Zhu, X.H., Zhu, X., and Dong, X.P. (2018). A negative feedback regulation of mTORC1 activity by the lysosomal Ca(2+) channel MCOLN1 (mucolipin 1) using a CALM (calmodulin)-dependent mechanism. *Autophagy* 14, 38–52. <https://doi.org/10.1080/15548627.2017.1389822>.
80. Xu, M., Zhong, X.Z., Huang, P., Jaślan, D., Wang, P., Sun, X., Weiden, E. M., El Hiani, Y., Grimm, C., and Dong, X.P. (2023). TRPML3/BK complex promotes autophagy and bacterial clearance by providing a positive feedback regulation of mTOR via PI3P. *Proc. Natl. Acad. Sci. USA* 120, e2215777120. <https://doi.org/10.1073/pnas.2215777120>.
81. Liu, B., Palmfeldt, J., Lin, L., Colaço, A., Clemmensen, K.K.B., Huang, J., Xu, F., Liu, X., Maeda, K., Luo, Y., and Jäättelä, M. (2018). STAT3 associates with vacuolar H(+)-ATPase and regulates cytosolic and lysosomal pH. *Cell Res.* 28, 996–1012. <https://doi.org/10.1038/s41422-018-0080-0>.
82. De Luca, M., Cogli, L., Progida, C., Nisi, V., Pascolutti, R., Sigismund, S., Di Fiore, P.P., and Bucci, C. (2014). RILP regulates vacuolar ATPase through interaction with the V1G1 subunit. *J. Cell Sci.* 127, 2697–2708. <https://doi.org/10.1242/jcs.142604>.

83. Hashimoto, Y., Shirane, M., and Nakayama, K.I. (2018). TMEM55B contributes to lysosomal homeostasis and amino acid-induced mTORC1 activation. *Genes Cells* 23, 418–434. <https://doi.org/10.1111/gtc.12583>.
84. Shin, J.J.H., Liu, P., Chan, L.J., Ullah, A., Pan, J., Borchers, C.H., Burke, J. E., Stefan, C., Smits, G.J., and Loewen, C.J.R. (2020). pH Biosensing by PI4P Regulates Cargo Sorting at the TGN. *Dev. Cell* 52, 461–476. <https://doi.org/10.1016/j.devcel.2019.12.010>.
85. Mulligan, R.J., Magaj, M.M., Digilio, L., Redemann, S., Yap, C.C., and Winckler, B. (2024). Collapse of late endosomal pH elicits a rapid Rab7 response via V-ATPase and RILP. Preprint at bioRxiv. <https://doi.org/10.1101/2023.10.24.563658>.
86. Xu, H., and Ren, D. (2015). Lysosomal physiology. *Annu. Rev. Physiol.* 77, 57–80. <https://doi.org/10.1146/annurev-physiol-021014-071649>.
87. Kilpatrick, B.S., Yates, E., Grimm, C., Schapira, A.H., and Patel, S. (2016). Endo-lysosomal TRP mucolipin-1 channels trigger global ER Ca²⁺ release and Ca²⁺ influx. *J. Cell Sci.* 129, 3859–3867. <https://doi.org/10.1242/jcs.190322>.
88. Thakore, P., Pritchard, H.A.T., Griffin, C.S., Yamasaki, E., Drumm, B.T., Lane, C., Sanders, K.M., Feng Earley, Y., and Earley, S. (2020). TRPML1 channels initiate Ca(2+) sparks in vascular smooth muscle cells. *Sci. Signal.* 13, eaba1015. <https://doi.org/10.1126/scisignal.aba1015>.
89. Scorzà, S.I., Milano, S., Saponara, I., Certini, M., De Zio, R., Mola, M.G., Procino, G., Carmosino, M., Moccia, F., Svelto, M., and Gerbino, A. (2023). TRPML1-Induced Lysosomal Ca(2+) Signals Activate AQP2 Translocation and Water Flux in Renal Collecting Duct Cells. *Int. J. Mol. Sci.* 24, 1647. <https://doi.org/10.3390/ijms24021647>.
90. Ko, J., Park, H., Heo, L., and Seok, C. (2012). GalaxyWEB server for protein structure prediction and refinement. *Nucleic Acids Res.* 40, W294–W297. <https://doi.org/10.1093/nar/gks493>.
91. Emsley, P., and Cowtan, K. (2004). Coot: model-building tools for molecular graphics. *Acta Crystallogr. D Biol. Crystallogr.* 60, 2126–2132. <https://doi.org/10.1107/s0907444904019158>.
92. Kimura, S., Noda, T., and Yoshimori, T. (2007). Dissection of the autophagosome maturation process by a novel reporter protein, tandem fluorescent-tagged LC3. *Autophagy* 3, 452–460. <https://doi.org/10.4161/auto.4451>.
93. Walton, Z.E., Patel, C.H., Brooks, R.C., Yu, Y., Ibrahim-Hashim, A., Riddle, M., Porcu, A., Jiang, T., Ecker, B.L., Tameire, F., et al. (2018). Acid Suspends the Circadian Clock in Hypoxia through Inhibition of mTOR. *Cell* 174, 72–87. <https://doi.org/10.1016/j.cell.2018.05.009>.
94. Cho, E.B., Yoo, W., Yoon, S.K., and Yoon, J.B. (2018). β-dystroglycan is regulated by a balance between WWP1-mediated degradation and protection from WWP1 by dystrophin and utrophin. *Biochim. Biophys. Acta. Mol. Basis Dis.* 1864, 2199–2213. <https://doi.org/10.1016/j.bbadiis.2018.04.001>.
95. Williamson, C.D., Guardia, C.M., De Pace, R., Bonifacino, J.S., and Saric, A. (2022). Measurement of Lysosome Positioning by Shell Analysis and Line Scan. *Methods Mol. Biol.* 2473, 285–306. https://doi.org/10.1007/978-1-0716-2209-4_19.
96. Saric, A., Freeman, S.A., Williamson, C.D., Jarnik, M., Guardia, C.M., Fernandopulle, M.S., Gershlick, D.C., and Bonifacino, J.S. (2021). SNX19 restricts endolysosome motility through contacts with the endoplasmic reticulum. *Nat. Commun.* 12, 4552. <https://doi.org/10.1038/s41467-021-24709-1>.
97. Thomas, J.A., Buchsbaum, R.N., Zimniak, A., and Racker, E. (1979). Intracellular pH measurements in Ehrlich ascites tumor cells utilizing spectroscopic probes generated in situ. *Biochemistry* 18, 2210–2218. <https://doi.org/10.1021/bi00578a012>.
98. Miesenböck, G., De Angelis, D.A., and Rothman, J.E. (1998). Visualizing secretion and synaptic transmission with pH-sensitive green fluorescent proteins. *Nature* 394, 192–195. <https://doi.org/10.1038/28190>.
99. Peng, T., Thorn, K., Schroeder, T., Wang, L., Theis, F.J., Marr, C., and Navab, N. (2017). A BaSiC tool for background and shading correction of optical microscopy images. *Nat. Commun.* 8, 14836. <https://doi.org/10.1038/ncomms14836>.

STAR★METHODS

KEY RESOURCES TABLE

REAGENT or RESOURCE	SOURCE	IDENTIFIER
Antibodies		
Anti-ARL8B	ThermoFisher Scientific	PA5-100124
Anti-RNF13	Cusabio	CSB-PA019831DSR1HU
Anti-FLAG	Sigma	F7425
Anti-HA	Santa Cruz Biotechnology	sc-7392
Anti-β-actin	GeneTex	GT5521
Anti-ALG-2	Santa Cruz Biotechnology	sc-376950
Anti-GADPH	Santa Cruz Biotechnology	sc-166574
Anti-LC3	MBL	PM036
Anti-p62	Novus Biologicals	H00008878
Anti-Ub	Santa Cruz Biotechnology	sc-166553
Anti-ARL8B	Proteintech	13049-1-AP
Anti-TRPML1	Alomone Labs	ACC-081
Anti-TRPML3	Alomone Labs	ACC-083
Anti-Lamp1	Santa Cruz Biotechnology	sc-18821
Chemicals, peptides, and recombinant proteins		
Lipofectamin 2000	Invitrogen	11668500
Lipofectamine RNAiMax	Invitrogen	13778150
MES	Sigma	M8250
HEPES	Sigma	H6147
ML-SA1	Sigma	SML0627
Torin 1	Cayman Chemical	CAY10997
ML-SI3	MedChemExpress	HY-139426
Penicillin-streptomycin	GenDEPOT	CA005-010
Blasticidin	InvivoGen	ant-bl-05
Puromycin	Enzo Life Sciences	BML-GR312-0050
Hygromycin B	InvivoGen	ant-hg-1
SN-2	MedChemExpress	HY-16696
Nigericin solution	Sigma	SML1997
Lysosensor DND-189	Invitrogen	L7535
Thapsigargin	Sigma	T9033
RNAiso Plus	Takara	9109
anti-FLAG M2 affinity gel	Sigma	A2220
Dynabeads® Protein G	Thermo Fisher Scientific	10003D
TB Green Premix Ex Taq	Takara Bio	RR420A
EBSS	Welgen	LB002-03
FBS	GenDEPOT	F0900-050
Critical commercial assays		
Ubiquitin IP Assay	Cytoskeleton, Inc	BK161
cDNA Synthesis Kit	Takara Bio	6210
Deposited data		
Original western blot images and microscopy data	This paper; Mendeley Data	DOI: https://doi.org/10.17632/bws7rpnt2w.1

(Continued on next page)

Continued

REAGENT or RESOURCE	SOURCE	IDENTIFIER
Experimental models: Cell lines		
HeLa	Korean Cell Line Bank	10002
HEK293T	Korean Cell Line Bank	N/A
MCF7	Korean Cell Line Bank	30022
HAP-1	Horizon	N/A
HeLa RNF13 shRNA	This paper	N/A
HeLa RNF167 shRNA	This paper	N/A
mRFP-GFP-LC3	Dr. M. Komatsu (Juntendo Univ)	N/A
HeLa ARL8B-mCherry and LAMP1-GFP	This paper	N/A
HeLa mCherry-SEpHluorin	This paper	N/A
HeLa mTFP1-hLAMP1-mCherry	This paper	N/A
HeLa GCaMP6f	This paper	N/A
Oligonucleotides		
Primers used for cloning and site-directed mutagenesis, and oligonucleotides used for complex reconstitution are listed in Table S1	This paper	Table S1
Recombinant DNA		
Plasmid: pcDNA3.1	Invitrogen	N/A
Plasmid: pFUGW-FIRE-pHLy	Addgene	170774
Plasmid: pCDH-CMV-MCS-EF1-Hygro	System Biosciences	CD515B-1
Plasmid: pCDH-CMV-MCS-EF1-Neo	System Biosciences	CD514B-1
Plasmid: pLKO.1 puro	Addgene	10878
Plasmid: peGFP-mCherry-SEpHluorin	Addgene	32001
Plasmid: pLX304-GCaMP6f	Addgene	163045
cDNA ARL8B	DNASU Plasmid Repository	NM_018184.2
cDNA RNF13	DNASU Plasmid Repository	NM_007282.4
cDNA ALG-2	Korean Human Genebank	hMU001447
Software and algorithms		
Prism 8	GraphPad	https://www.graphpad.com/scientific-software/prism/
Fiji/ImageJ	Fiji/ImageJ	N/A
GalaxyWEB	Ko et al. ⁹⁰	https://galaxy.seoklab.org/
COOT	Emsley et al. ⁹¹	https://www2.mrc-lmb.cam.ac.uk/personal/emsley/coot/
Biorender	Biorender	https://www.biorender.com/
Microsoft Excel	Microsoft	https://www.microsoft.com/

EXPERIMENTAL MODEL AND STUDY PARTICIPANT DETAILS**Cell culture**

HeLa, HEK293T, and MCF7 cells were cultured in high-glucose Dulbecco's modified Eagle's medium (DMEM) (WelGENE) supplemented with 10% fetal bovine serum (FBS) (GenDEPOT) and 1% penicillin/streptomycin at 37°C with 5% CO₂. HAP-1 (TRPML1-KO, TRPML3-KO, and WT) cells were purchased from Horizon and cultured in Iscove's modified Dulbecco's medium (Sigma) supplemented with 10% FBS, 4 mM L-Glutamine, 1 mM sodium pyruvate, and 1% antibiotics. A cell line expressing mRFP-GFP-LC3, was a kind gift from Dr. M. Komatsu (Juntendo Univ),⁹² and cells were cultured in DMEM supplemented with 10% FBS and 1% penicillin/streptomycin. Cell lines underwent regular mycoplasma screening, with no contamination detected.

METHOD DETAILS**Plasmids**

The clones for the complementary DNAs (cDNAs) encoding human *ARL8B* (accession no. NM_018184.2) and *RNF13* (accession no. NM_007282.4) were obtained from DNASU Plasmid Repository. The plasmid for the expression of epitope-tagged *ARL8B* was constructed by subcloning the PCR-amplified cDNA into the in-house modified pcDNA3.1 (Invitrogen), which has a C-terminal FLAG- or HA-tag as described.²⁵ The full-length complete coding sequence of *RNF13* and the deletion mutants for *RNF13* were generated by subcloning each PCR-amplified cDNA into the modified pcDNA3.1 or pYR, generating plasmid constructs with the C-terminal FLAG, or HA-tag using Clal and XbaI restriction sites. To generate *RNF13* Δ205–237, two specific fragments of *RNF13* including 1–204, and 238–381 were generated with unique primers: fragment 1–204 with *RNF13* FL sense primer and *RNF13* 1–204 antisense-1 primer, and fragment 238–381 with *RNF13* 238–381 sense primer and *RNF13* FL antisense primer. To generate *RNF13* Δ205–219, two specific fragments of *RNF13* including 1–204 and 220–381 were generated: fragment 1–204 with *RNF13* FL sense primer and *RNF13* 1–204 antisense-2 primer, and fragment 220–381 with *RNF13* 220–381 sense primer and *RNF13* FL antisense primer. To generate *RNF13* Δ220–233, two specific fragments of *RNF13* including 1–219 and 234–381 were generated with unique primers: fragment 1–219 with *RNF13* FL sense primer and *RNF13* 1–219 antisense primer, and fragment 234–381 with *RNF13* 234–381 sense primer and *RNF13* FL antisense primer. After generating the two specific fragments, they were joined using overlap extension PCR with the *RNF13* FL primer set. To generate *RNF13N/RNF128C*, the N-terminal of *RNF13* was fused to the C-terminal of *RNF128*, and *RNF128N/RNF13C* were generated by fusing N-terminal of *RNF128* with the C-terminal of *RNF13*. The point mutation constructs including C243S, R210,214A, R215,217A, K220A, K220,224A, K220,224,233A (3KA), D291,293,295,297A (4DA), H308A, H332A, H332K, H361A, L311S, L312P, L311,312A, and E309,L311,L312A were generated using QuikChange Kit following the manufacturer's protocol (Stratagene). To generate the plasmid expressing siRNA-resistant full-length *RNF13*, we introduced three single-nucleotide mutations (T300G, T303C, and T306C) in the coding sequence without causing any changes in amino acids (sense mutation) using QuikChange Kit (Stratagene). The *ARL8B* mutant constructs, K131R, K141R, and K146R, were generated using the QuikChange Kit according to the manufacturer's protocol (Stratagene). The cDNA clone for *ALG-2* was obtained from the Korean Human Genebank (hMU001447). The epitope-tagged *ALG-2* was generated by subcloning the PCR-amplified cDNA into the modified pcDNA3.1 with C-terminal FLAG or HA tags using BgIII and XbaI sites. The *ALG-2* mutant constructs, E47A or E114A, were generated using QuikChange Kit following the manufacturer's protocol (Stratagene). To generate the *ARL8B-mCherry* construct, the fusion construct of the *ARL8B* and mCherry was first created by the *ARL8B* cDNA and the mCherry cDNA from the pFUGW-FIRE-pHLY plasmid (Addgene #170774)⁵⁹ via jumping PCR amplification. Then, the resulting PCR product was subcloned into the pCDH-CMV-MCS-EF1-Hygro vector using NheI and BamHI restriction enzymes. To generate the *LAMP1-GFP* fusion construct, the *LAMP1* cDNA was first inserted into the pEGFP-N1 vector using NheI and AgeI restriction sites. The *LAMP1-GFP* fusion construct was then cloned into the pCDH-CMV-MCS-EF1-Neo vector using NheI and BamHI restriction sites. All constructs were confirmed by sequencing. The primer sequences used for cloning and the vectors cloned into are listed in Table S1.

RNAi

SiRNAs against *RNF13*, *ARL8B*, *ALG-2*, *RNF167*, *TRPML1*, and *TRPML3* were generated (Bioneer) and transfected using Lipofectamine RNAiMax reagent (Invitrogen) according to the manufacturer's instructions. For knockdown experiments, cells were transfected with 60 nM siRNA for 72 h for *RNF13*, *ARL8B*, *ALG-2*, and *RNF167*. For knockdown of *TRPML1* and *TRPML3* expression, cells were transfected with 60 nM siRNA for 24 h, followed by 20 nM siRNA transfection for another 48 h. The sense siRNA sequence were as follows: si*RNF13*#1, 5'-UUAGAACUUGAUUGUA-3'; si*RNF13*#2, 5'-GAAACUUCCUGUACAUAAA-3'; si*RNF13*#3, 5'-GCCAC CUUAUCUUAGUUCAG-3'; si*ARL8B*, 5'-AGGUACGUCACAAUAGAU-3'; si*ALG-2*, 5'-AAAGACAGGAGUGGAGUGAUAC AG-3'; si*RNF167*, 5'-UAGCUCGUUGUAUCCAGCACCGGAA-3'; si*TRPML1*, 5'-CCACAUCCAGGAGUGUAA-3'; and si*TRPML3*, 5'-GGAUGGUACAUUAUGAUUAUU-3'.

RNA extraction and quantitative real-time PCR (qRT-PCR)

Total RNA was extracted from cells using Trizol Reagent (Invitrogen, Carlsbad, USA) according to the manufacturer's protocol. Complementary DNA (cDNA) was synthesized using a cDNA synthesis kit (Takara, Shiga, Japan). qRT-PCR was performed using an SYBR Green qRT-PCR analysis kit (Takara, Shiga, Japan). Messenger RNA (mRNA) levels of *RNF167* were quantified using the 2^{-ΔΔ}Ct method, with GAPDH mRNA as the reference gene. Primers for *RNF167* are as follows: 5'-TCC AGG GGT TCC TTG TGG A-3' (sense) and 5'-CCT TCT GGG CAT TTA GGA CCT T-3' (antisense). Primers for GAPDH are as follows: 5'-AACTTGCGATTGTG GAAGG-3' (sense), and 5'-ACACATTGGGGTAGGAACA-3' (antisense).

Cell line generation

To generate *RNF13* or *RNF167* knockdown cell lines, HEK293T cells were co-transfected with psPAX2, PMD2.G and either pLKO.1-sh*RNF13*-puro or pLKO-sh*RNF167*-puro using Lipofectamine 2000 transfection reagent. The pLKO.1-sh*RNF13*-puro and pLKO.1-sh*RNF167*-puro plasmids were constructed by subcloning the oligonucleotides listed in Table S1 into pLKO.1 puro (Addgene, #10878). Lentivirus-containing media were collected 72 h post-transfection and used for the transduction of HeLa and MCF7 cells in the presence of 10 µg/mL polybrene (Sigma). The medium was changed to complete DMEM supplemented with 1 µg/mL

puromycin at 72 h post-transduction. Selection continued for 2 days until complete infection was achieved. The cells were cultured and used for subsequent experiments.

To generate HeLa cells stably expressing both ARL8B-mCherry and LAMP1-GFP, cells were first transduced with lentivirus containing the plasmid encoding *ARL8B-mCherry* for 72 h. After selection with hygromycin continued for additional 5 days, the cells were transduced with lentivirus carrying the plasmid encoding *LAMP1-GFP*. Selection was continued with G418 for an additional 5 days until stable expression was achieved.

The sensor cell lines for relative measurement of pH_i, pH_{lys}, and cytosolic Ca²⁺ levels were generated in a HeLa cell background. For measuring pH_i, pCDH-Hygro-mCherry-SEpHluorin plasmid was constructed by subcloning the DNA fragment encoding mCherry-SEpHluorin (Addgene, #32001)⁵⁷ into pCDH-CMV-MCS-EF1 α-Hygro (System Biosciences, #CD515-1) using XbaI and BamHI sites. This construct includes mCherry and SuperEcliptic (SE) pHluorin, which are pH-insensitive and pH-sensitive, respectively. Cell lines stably expressing mCherry-SEpHluorin (pH_i cell line), FIRE-pHLY (pH_{lys} cell line), or GCaMP6f (cytosolic Ca²⁺ cell line) were generated by lentiviral transduction. HEK293T cells were transfected with pCDH-Hygro-mCherry-SEpHluorin, pFUGW-FIRE-pHLY (Addgene, #170774),⁵⁹ or pLX304-GCaMP6f (Addgene, #163045)⁶¹ with psPAX2, and PMD2.G using Lipofectamine 2000 for 72 h. The lentivirus was transduced into HeLa cells in the presence of 10 µg/mL polybrene for 72 h. Cells were selected using 200 µg/mL hygromycin B for the pH_i cell line and 10 µg/mL blasticidin for the cytosolic Ca²⁺ cell line. For the pH_{lys} cell line, cells were used for the subsequent experiments immediately after a 72-h transduction with lentiviral medium without selection, due to the high toxicity of zeocin to the transduced cells.

Cell transfection and treatment

Lipofectamine RNAiMax (Invitrogen) or polyethylenimine (Sigma) were used for the transfection of cell lines. MG132 and Torin1 were purchased from Caymen Chemical Company, Bafilomycin A1, ML-SA1, ML-SI3, and thapsigargin from Sigma, and SN-2 from MedChemExpress.

For starvation experiments, cells were cultured in complete media for 48 h before undergoing starvation, following previously described protocols.⁵⁵ For starvation experiments, two different conditions were used. For complete nutrient deprivation, cells were washed with phosphate-buffered saline (PBS) and incubated in EBSS (Welgen) at 37°C with 5% CO₂ for the duration specified in the figure legends. For milder starvation, cells were washed with PBS and incubated in serum-free DMEM at 37°C with 5% CO₂ for the indicated duration in figure legends.

To establish stable acidic or alkaline pH conditions, media formulations were prepared as described in a previous study.⁹³ DMEM (Gibco) containing 25 mM glucose and 4 mM L-glutamine was supplied with 5% FBS, 0.25× penicillin-streptomycin, and 25 mM MES (pKa 6.66 at 37°C, useful pH range of 6.1–7.5 at 25°C, Sigma), or 25 mM HEPES (pKa 7.31 at 37°C, useful pH range of 6.8–8.2 at 25°C, Sigma), or 25 mM Tris (pKa 7.72 at 37°C, useful pH range of 7.2–9.0 at 25°C, Sigma). Media were adjusted to pH 6.5, 7.5, or 8.5 using NaOH or HCl before filter sterilization and used in atmospheric CO₂.

Identification of ARL8B as a potential RNF13 substrate using proximity-dependent biotin labeling

HeLa cells were transfected with the constructs encoding RNF13-BirA-FLAG and AP-HA-Ub for 24 h and then treated with 50 µM Biotin and 25 µM MG132 for 4 h. Purification of the biotinylated-ubiquitinated proteins was performed as described previously.^{53,94} Briefly, cells were harvested and lysed in the homogenization buffer (0.25 M sucrose, 10 mM HEPES, pH 7.4, 1 mM EDTA, 10 mM PMSF, and 10 mM NEM). Cell lysates were centrifuged for 60 min at 28000 xg to collect membrane-enriched fraction, which was subsequently solubilized in lysis buffer (2% SDS, 250 mM NaCl, 50 mM Tris-Cl, pH 7.4). The lysates were boiled at 95°C for 10 min, centrifuged for 10 min at 12000 xg, and incubated with anti-FLAG M2 affinity gel overnight at 4°C. The lysates containing biotinylated proteins were incubated with streptavidin agarose in a buffer (250 mM NaCl, 50 mM Tris-Cl, pH 7.4) overnight at 4°C. Subsequently, beads were reduced, alkylated, and trypsinized into peptides. Finally, trypsinized peptides were purified using ubiquitin branch motif (K-ε-GG) immunoaffinity beads (Cell Signaling Technology) and analyzed using nanoelectrospray LC-ML/MS on an LTQ Orbitrap Velos (Thermo Fisher Scientific) as described previously.^{53,94} For matching proteins using MS/MS spectra in Mascot (Matrix Science), the following parameters were used: 2 missed cleavage sites was chosen, carbamidomethyl (C) as fixed modification, monoisotopic for mass value, protein mass unrestricted, 10 ppm for peptide mass tolerance, and 0.8 Da for fragment mass tolerance.

Co-immunoprecipitation and western blot analysis

HeLa cells were cultured for 24 h post-transfection with the indicated plasmids, then harvested by trypsinization, followed by washing and centrifugation. Cells were immediately placed in lysis buffer [50 mM Tris-HCl (pH 7.4), 150 mM NaCl, 1 mM EDTA, 1% Nonidet P-40, 1 mM dithiothreitol, and 0.2 mM PMSF] for 30 min on ice. Cell lysates were either analyzed directly by western blot analysis or processed further for co-immunoprecipitation (Co-IP) experiments. Co-IP was conducted as follows: lysates were centrifuged at 21000 xg for 15 min at 4°C; the supernatants were then incubated with anti-FLAG M2 affinity gel (Sigma) overnight at 4°C; after brief centrifugation at 1500 rpm, the pellets were washed with lysis buffer containing 0.5% NP40 and the immunoprecipitated proteins were eluted by incubating the pellets with SDS sample buffer (200 mM Tris-Cl (pH 6.8), 2% SDS, 0.4% bromophenol blue, and 40% glycerol) for 30 min at 37°C. For immunoprecipitation with anti-ALG-2 or anti-RNF13 antibodies, cell lysates were incubated with the antibodies in the presence of 5 mM EGTA or 100 µM CaCl₂ overnight at 4°C. The lysates were then incubated with

Dynabeads Protein G for 2 h at 4°C. The beads were washed with lysis buffer and subsequently processed for western blot analysis. Protein samples were separated by SDS-polyacrylamide gel electrophoresis, transferred onto nitrocellulose membranes (Pall Corp., Pensacola, FL), and subjected to western blot analysis. The band was visualized using the ECL system (DonginBiotech, Seoul, Korea).

Ubiquitination assay

HeLa cells were transfected with a plasmid encoding T7-ubiquitin along with the expression constructs specified in the figure legends. After 24 h, the transfected cells were treated with 25 µM MG132 for 6 h. The cells were then harvested and lysed using a lysis buffer. The lysates were centrifuged at 21000 × g for 15 min at 4°C to remove cell debris. The resulting supernatants were incubated with anti-FLAG M2 affinity gel (Sigma) overnight at 4°C. After centrifugation, the pellets were washed with lysis buffer, eluted in SDS sample buffer, and analyzed by western blot analysis.

Ubiquitination of endogenous ARL8B was analyzed using the SignalSeeker Ubiquitination Detection Kit (Cytoskeleton) following the manufacturer's instruction. Briefly, HeLa cells were transfected with the indicated constructs or treated with the specified conditions as described in the figure legends. Cell lysates were washed, incubated with BlastR lysis buffer (with NEM and protease inhibitor), passed through a BlastR filter, and diluted with BlastR dilution buffer. They were then incubated with control or ubiquitination affinity beads for 2 h at 4°C, washed with BlastR-2 buffer, and eluted with bead elution buffer. Finally, samples were collected using spin columns and processed for western blot analysis.

Immunofluorescence microscopy

Cells grown on coverslips were washed with PBS and fixed in 4% paraformaldehyde for 15 min. Cells were permeabilized with 0.5% PBS-T (0.5% Triton X-100 in PBS) for 5 min, washed with 0.1% PBS-T, and blocked with 10% normal goat serum for 30 min. Samples were incubated with primary antibody overnight at 4°C. Cells were washed three times with 0.1% PBS-T before incubating with fluorescently conjugated secondary antibody for 50 min. Finally, cells were washed with 0.1% PBS-T, and nuclei were stained with DAPI. Immunofluorescence images were obtained using a confocal laser scanning microscope (LSM 700 or LSM800; Zeiss, Gottingen, Germany) or an inverted fluorescence microscope (LSM510; Carl Zeiss, Germany).

Time-lapse confocal imaging

HeLa cells stably expressing ARL8B-mCherry and LAMP1-GFP were seeded onto an SPL confocal dish. Time-lapse fluorescence imaging was performed using an Olympus FV3000 scanning confocal microscope equipped with a 60 × 1.42 NA oil immersion objective at room temperature. Cells were incubated in a HEPES-buffered media, washed twice with PBS, and placed under the specified conditions. A 488 nm Diode laser was used to excite GFP, and fluorescence emission was collected between 500 and 540 nm using a GaAsP PMT detector in analog mode. Similarly, a 561 nm Diode laser was used to excite mCherry, with emission collected between 570 and 620 nm using the same detector. A series of sequential images at 12 bits were collected and images were obtained over 1 h period with a frame time of 1 min ($N = 60$).

Fluorescence signal intensity was quantified by measuring mCherry signals in the cell undergoing time-lapse imaging every minute for 1 h using ImageJ. The relative signal for plotting was calculated as the decrease from the initial signal, normalized to the original value.

Analysis of intracellular distribution of lysosomes

To analyze lysosome distribution, we used a "shell analysis" method,⁹⁵ utilizing confocal images acquired with a Zeiss LSM800 inverted laser scanning microscope (Carl Zeiss). The images were processed using FIJI as described previously.^{31,95,96} For accurate quantification, we selected cells with a relatively round and uniform shape, excluding narrow, elongated cells due to potential inaccuracies in analysis. These criteria were predefined and applied consistently across all conditions.

Cell boundaries were determined using the CD147 marker, which localizes both intracellularly and at the plasma membrane, while nuclear boundaries were defined by the DAPI signal. The LAMP1 signal from neighboring cells was excluded, and the total whole-cell LAMP1 signal was quantified. The nuclear outline was then expanded in fixed increments five times to create five concentric shells (areas). The LAMP1 signal was determined in each shell. Area 1 was defined as the perinuclear region of the cell, while Areas 4 and 5 were defined as the peripheral edge. Each cell was analyzed individually. For each condition, three independent experiments were conducted, with more than 20 cells per experiment. The ratio of perinuclear lysosomes was calculated as the LAMP1 signal in Area 1 divided by the total LAMP1 signal. Quantifications were confirmed by a researcher blinded to the experimental groups.

Measurement of pH_i and pH_{lys}

The pH_i was assessed using HeLa cells stably expressing mCherry-SEpHluorin (pH_i sensor cell line), which contains the pH-sensitive fluorescent protein SEpHluorin (green) fused with the pH-insensitive mCherry (red). A standard curve was generated by determining the green to red signal intensity ratio at various pH. Briefly, cells were washed twice with PBS and incubated in a high-potassium buffer to prevent a [K⁺] gradient from driving a proton gradient.^{97,98} The buffer contained (in mM): KCl 100, NaCl 38, CaCl₂ 1.8, MgSO₄ 0.8, and NaH₂PO₄ 0.9, with Good buffer (25 mM) pre-adjusted to pH 8.0, 7.5, 7.0, 6.5, and 6.0, along with 10 µm nigericin (Invitrogen). The Good buffer was chosen based on its pKa with MES for pH 6.5; HEPES for pH 7.0 and pH 7.5; and Tris for

pH 8.0 and pH 8.5. Cells were cultured in complete DMEM for 48 h, then washed twice with PBS and treated as indicated in the figure legends. Images of 20 \times fields were captured using an Olympus IX70 inverted fluorescence microscope. Before calculating the SEpHluorin/mCherry ratio, images were corrected for background and shading using a BaSiC tool in the Fiji plugin.⁹⁹ Three replicates per experiment, with at least three fields analyzed per replicate, were used to calculate the mean pH_i \pm SD.

The pH_{lys} was assessed using HeLa cells stably expressing mTFP1–hLAMP1–mCherry. This construct contains a pH-sensitive mTFP1 fused to the lysosomal lumen-facing N-terminal portion of human LAMP1, and a pH-insensitive mCherry fused to the C-terminal of hLAMP1, facing outside the lysosome.⁵⁹ A standard curve was generated as described previously. The buffer composition included (in mM): NaCl 5, KCl 115, MgSO₄·7H₂O 1.3, and MES 25, pre-adjusted to a pH range of 3.0–6.0, along with 10 μ M nigericin. Images of 20 \times fields were captured using an Olympus IX70 inverted fluorescence microscope. Cell boundaries were determined using the free hand selection tool in Fiji. The signals of mTFP1 (green) and mCherry (red) were measured by subtracting the background signal from the whole-cell signal. The ratio of mTFP1/mCherry was then calculated. At least 20 representative cells with three replicates were analyzed.

Measurement of lysosomal pH using lysosensor staining

For the lysosensor assay, cells were plated overnight in a 35-mm confocal cell culture dish or 96-well black plate. The following day, cells were treated with different conditions as described in the figure legends, and 2 μ M Lysosensor DND-189 (Invitrogen) was applied for 1 h. To generate a pH standard calibration curve, cells were incubated for 10 min at 37°C in sodium acetate-acetic acid calibration buffers (from pH 4 to pH 5.5). To clamp lysosomal pH, 10 μ M nigericin and 1 mM KCl were added. The fluorescence of the lysosensor was observed with a confocal microscope (LSM800W/Airys-can, Carl Zeiss), and the fluorescence intensity was quantified with a fluorometer (Bio-Tek, Winooski, USA).

Measurement of cytoplasmic Ca²⁺ levels

HeLa cells stably expressing GCaMP6f were grown for 48 h and incubated under different conditions as described in the figure legends. The images of 20 \times fields were captured using an Olympus IX70 inverted fluorescence microscope and corrected for background using Fiji. The fluorescence intensity of GCaMP6f (F) was monitored. Results are presented as $\Delta F/F_0$, where F₀ is the baseline fluorescence and ΔF is the changes in fluorescence ($\Delta F = F - F_0$). Three replicates per experiment, with at least three fields analyzed per replicate, were used to calculate the mean $\Delta F/F_0 \pm$ SD.

Molecular docking and refinement

The crystal structure of the RNF13 RING domain (PDB entry: 5ZC4) and the primary structure of the RNF13 acidic-rich region (aa. 291–305) were prepared for molecular docking. Molecular docking was conducted using GalaxyWEB (<https://galaxy.seoklab.org>).⁹⁰ The RNF13 helical region (aa. 205–215) was extracted from the AlphaFold structure.⁴⁵ The connection between them was established using COOT,⁹¹ followed by refinement using GalaxyWEB.

QUANTIFICATION AND STATISTICAL ANALYSIS

GraphPad Prism v8.8 (San Diego, CA) and Microsoft Excel were used for calculations, analyses, and data visualization. Data are presented as mean \pm SD. Statistical significance was assessed using an unpaired Student's t-test, one-way analysis of variance (ANOVA), or two-way ANOVA, as detailed in the corresponding figure legends. Figures 1E, 1H, 4A, and others feature SuperPlots. These plots display individual data points as small circles, the means of each independent experiment as large, color-coded circles, and the mean \pm SD of these means as a bar. Differences were considered statistically significant at * $p < 0.05$, ** $p < 0.01$, or *** $p < 0.001$; "ns" denotes no significant difference. Quantifications and statistical analyses were based on three independent replicates, with over 20 cells observed in each replicate.